PHYSICAL REVIEW B **109**, 054101 (2024)

Picometer atomic displacements behind ferroelectricity in the commensurate low-temperature phase in multiferroic YMn_2O_5

Tina Weigel,[1] Carsten Richter,[2] Melanie Nentwich,[3] Erik Mehner,[1] Valentin Garbe,[4] Laurence Bouchenoire,[5,6]
Dmitri Novikov,[3] Dirk C. Meyer,[1] and Matthias Zschornak[1]
[1]*Institute of Experimental Physics, Technical University Bergakademie Freiberg, 09596 Freiberg, Germany*
[2]*Leibniz-Institut für Kristallzüchtung, 12489 Berlin, Germany*
[3]*Deutsches Elektronen-Synchrotron DESY, 22607 Hamburg, Germany*
[4]*Institute of Applied Physics, Technical University Bergakademie Freiberg, 09596 Freiberg, Germany*
[5]*XMaS/BM28, European Synchrotron Radiation Facility, 38043 Grenoble, France*
[6]*University of Liverpool, Department of Physics, Liverpool L69 7ZE, England, United Kingdom*

(Received 11 July 2023; revised 20 November 2023; accepted 12 December 2023; published 1 February 2024)

Multiferroics are rare materials that exhibit an interaction of ferroelectricity and magnetism. One such multiferroic material is the Mn-based mullite YMn_2O_5. YMn_2O_5 undergoes several low-temperature phases, and the origin of ferroelectricity in the commensurate phase remains open. Changes in the Mn spin configuration are believed to be the main driving force, which can be induced by magnetostriction caused by symmetric exchange, the antisymmetric inverse Dzyaloshinskii-Moriya interaction, or a combination of both. These mechanisms are accompanied by specific displacements of ions in the structure. The space group *Pbam* (55) of the paraelectric phase does not allow polar displacements. Moreover, conventional structure analysis has been unsuccessful in refining the charge structure in a lower symmetric phase due to its limited sensitivity in resolving the expected positional displacements. To shed light on this controversial discussion, our goal was to resolve potential ionic displacements within a polar space group by employing the new *resonantly suppressed diffraction* method, which is highly sensitive to minuscule structural changes in the (sub)picometer range. In this paper, we present the first refined structure model of the commensurate phase in YMn_2O_5 using the lower symmetric space group $Pb2_1m$, allowing polarization in the *b* direction. We observed a significant displacement of the Mn ions and the partial structure of oxygen, resulting in a calculated spontaneous polarization $P_S = (1.3 \pm 0.4)\,\mathrm{mC\,m^{-2}}$, which is in good agreement with our measured value $P_S = (0.88 \pm 0.06)\,\mathrm{mC\,m^{-2}}$. Importantly, we confirm that P_S predominantly arises from an ionic contribution induced by magnetostriction. These results hold great interest not only for all multiferroic Mn-based mullites, but also for other multiferroic materials where ferroelectricity arises from their magnetic order. Furthermore, a precise understanding of the ionic movement induced by magnetism will aid in the material tuning process to enhance or create multiferroic properties.

DOI: 10.1103/PhysRevB.109.054101

I. INTRODUCTION

Multiferroics are rare materials, which combine ferroelectric and magnetic properties [1] and are interesting for memory devices [2], sensors [3], phase shifters [4], and energy harvesting [5]. According to Khomskii [6], two types of multiferroics exist. In type I multiferroics, ferroelectricity and magnetism occur at different temperatures and mechanisms, which leads to weak coupling between these properties. In type II multiferroics, the ferroelectricity only exists in a magnetically ordered state and is magnetically driven. A type II multiferroic material is YMn_2O_5 in its low-temperature phases. YMn_2O_5 is a manganese-based mullite [7], which crystallizes within the space group *Pbam* (55) (see Fig. 1; all crystal structures were produced using VESTA3 [8]) and is nonpolar at room temperature. Mn occupies two different Wyckoff positions in the unit cell, one with octahedral (center ion Mn^{4+}, Wyckoff site $4f$) and one with pyramidal (center ion Mn^{3+}, Wyckoff site $4h$) oxygen coordination [9]. Beside the multiferroic properties, YMn_2O_5 is interesting as a catalyst [10–12], as well.

The paramagnetic and paraelectric (P) YMn_2O_5 becomes multiferroic at low temperatures [13]. The material undergoes four phase transitions by lowering the temperature [14–16] (see Fig. 2). Below $T_{N_1} = 45\,\mathrm{K}$, the structure becomes antiferromagnetic with a two-dimensional incommensurate modulation (2D-ICM), but is still paraelectric. Ferroelectricity sets in at $T_D = 40\,\mathrm{K}$ with a one-dimensional incommensurately modulated (1D-ICM) magnetic phase between $T_D = 40\,\mathrm{K}$ and $T_{CM} = T_{C_1} = 39\,\mathrm{K}$. However, most articles only report either T_D or T_{CM} [16–20]. Between T_{CM} and $T_{N_2} = T_{C_2} = 19\,\mathrm{K}$ the magnetic structure becomes commensurately modulated (CM) along *c* with an electric polarization in the *b* direction. Below 19 K, the spontaneous polarization changes sign and the structure becomes weakly ferroelectric while the magnetic moments rearrange back into a two-dimensional incommensurate modulation (LT-2D-ICM).

The main focus of the present paper is understanding the structural changes occurring in the CM phase (i.e., between 19 and 39 K) where the electric polarization aligns along the *b* direction [21,22]. The CM phase is usually described contradictorily as ferroelectric within the crystallographic space

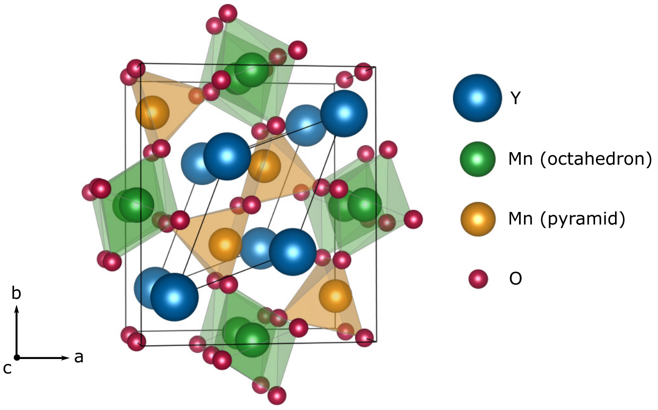

FIG. 1. Room temperature P phase of YMn_2O_5 with space group *Pbam* (55).

group *Pbam* (55), which is nonpolar and therefore prohibits ferroelectricity. Apparently, the atomistic origin of ferroelectricity in the CM phase is still not clear. Previous work favors two magnetically induced mechanisms based on changes in the Mn spin configuration: one caused by magnetostriction due to symmetric exchange [21,23,24], and the other one caused by the antisymmetric inverse Dzyaloshinskii-Moriya interaction [15,25], or a combination of both [15,26–28]. The mechanisms infer certain ionic displacements within the crystal structure. Some of the preceding articles on YMn_2O_5 reported on structural changes between the room temperature and the CM phase [16,18,29–33]. However, most work did not interpret these data and rather focused on the magnetic properties [13,14,16–18,21,24,25,27,34–45]. Others were explicitly searching for changes, but attempts to solve the structures of the CM phase were inconclusive [46,47]. Therefore, it is still unclear to what extent the ferroelectric transition can be evidenced in the crystal structure *Pbam* [32,33,48]. A possible polar structure for the CM phase is obtained by symmetry reduction to space group $Pb2_1m$ (26) (see Appendix A), which allows a polarization in the *b* direction. Additionally, this space group has already been theoretically proposed [22,29,49] but has not yet been experimentally observed in YMn_2O_5 with x-ray or neutron diffraction, because ionic displacements are much smaller than in typical displacive-type ferroelectrics [46].

In this paper, we use a recently developed *resonant x-ray diffraction* (RXD) technique [50] to enhance the sensitivity to atomic displacements and to shed light on this controversial discussion about the origin of ferroelectricity in YMn_2O_5. In general, RXD combines diffraction and core-hole spectroscopy. For investigations with RXD different physical aspects of the electronic resonance, such as enhanced elemental contrast [51,52] or polarization anisotropy, can be used. The latter gives information about the short-range order [53,54], magnetic properties [55,56], defect structures [53,57], or electronic properties [58,59]. Here, we make use of destructive interference in RXD, referred to as *resonantly suppressed diffraction* (RSD), to determine tiny atomic displacements [50]. RSD was demonstrated for the first time in the structural refinement of an electric-field induced polar surface layer in $SrTiO_3$ [50,60]. In the presented paper, we use the high sensitivity for atomic displacements of the RSD method to isolate the ionic contributions to the polarization in order to explain the origin of ferroelectricity in the CM phase.

II. METHODOLOGY

RSD is based on the work of Richter *et al.* [50] and uses resonantly tuned extinction evoked by the counterbalance of scattering contributions from different elements in the crystal structure. This effect is expressed by a vanishing structure factor and strongly depends on the crystal structure, the selected Bragg reflection, and the x-ray energy. Under such special conditions, the structure amplitude passes through a loop in the complex plane that passes through the origin and leads to a pronounced minimum in the intensity of a Bragg reflection. Small changes in atomic positions and thermal vibrations will shift the structure amplitude and the loop in the complex plane, with different effect in orthogonal directions, respectively. The specific directions depend on the position and form factor of the corresponding atom. The minimum position and intensity of the energy dependence are very sensitive to any structural change and provide excellent contrast to study atomic displacements on the picometer scale [50]. The general analysis procedure is illustrated in Fig. 3.

Following the main idea of the RSD concept, the selection of Bragg reflections is such that the diffraction intensity is minimized when scanning the x-ray energy across the absorption edge while the signal-to-noise ratio is maximized. The reflexes used for high-precision refinement of the structure are selected according to an optimized strategy to identify the most promising reflexes and improve the analysis procedure (see Fig. 3). Based on an initial guess of the structure, calculations of all the Bragg reflections yield sensitive candidates for the measurement (see Fig. 3, left). Possible sensitive reflections are reassessed in terms of contrast, location of the minimum, and parameter sensitivity. In the case of the presented paper, static displacements along the *b* direction

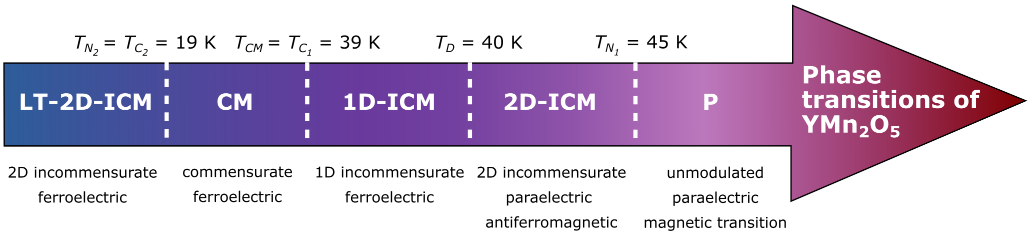

FIG. 2. Overview of the four low-temperature phase transitions of YMn_2O_5.

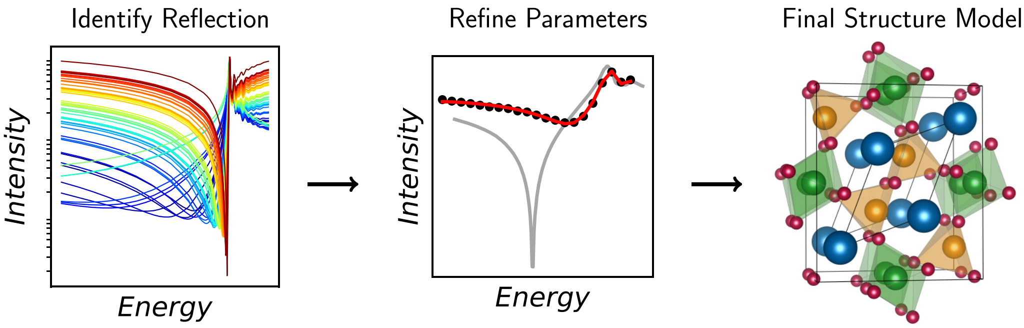

FIG. 3. General procedure of the structure solution within this paper. Left: Identification of sensitive reflections. Those reflections are characterized by a structure factor approaching zero and a respective local minimum of the energy dependent Bragg intensity, which provides orders of magnitude contrast. Middle: Refinement of the structural parameters based on the experimental data (black dots), in particular within the vicinity of the local energy minimum. The relevant dynamic and static atomic displacement parameters are determined by refining the sensitive reflections simultaneously. Even minuscule displacements can be revealed (gray, tabulated structure; red, refined fit). Right: Final model of the structure with subpicometer resolution of the atomic positions.

will manifest themselves particularly in reflections with a large momentum transfer along this direction, which is why these reflections are preferred. The selected reflections are subsequently reevaluated during the experiment, with each set of measured reflections or newly refined structural degree of freedom. This selection and evaluation of the sensitive reflections is not straightforward. In an iterative procedure [more details in Supplemental Material (SM) Sec. S I [61]; see also [62,63] therein], we analyzed the steadily acquired experimental data to obtain an updated list of reflections that are sensitive to prevailing parameter ambiguities.

The refinement of the structure is based on the fit of simulated RSD spectra to the experimental data to minimize differences, by varying both the structural degrees of freedom as well as the specific experimental parameters (see Fig. 3, middle). The relative deviation between the measured and calculated spectra was minimized using the PYTHON module LMFIT [64]. The residuals R were defined as the difference between simulated and experimental logarithmic intensities, equivalent to the assumption of a constant relative error. The simulated intensities are calculated using the kinematic approximation [65]

$$I_{\text{kin}} \propto A(E)|F(E,\boldsymbol{Q})|^2, \tag{1}$$

with the absorption factor $A(E) \approx 1/\mu(E)$ for thick crystals (μ the absorption coefficient), the photon energy E, the momentum transfer vector $\boldsymbol{Q}$, and the structure factor $F(E,\boldsymbol{Q})$. The latter is defined as

$$F(E,\boldsymbol{Q}) = \sum_{i=1}^{N} o_i f_i(E,\boldsymbol{Q}) \exp(-M_i) \exp(\mathrm{i}\boldsymbol{Q}\cdot\boldsymbol{r}_i), \tag{2}$$

with the N atoms i, their occupancies of the crystallographic sites o_i, their atomic scattering factors $f_i(E,\boldsymbol{Q})$, and their (static) positions in real space $\boldsymbol{r}_i$. The Debye-Waller factors $\exp(-M_i)$ are related to the atomic displacements $\boldsymbol{U}_i$ in the $\boldsymbol{Q}$ direction according to $M_i = {}^1\!/_2\langle(\boldsymbol{Q}\cdot\boldsymbol{U}_i)^2\rangle$ (dynamic displacement parameters or atomic displacement parameters (ADPs)), i.e., the mean square projections of the atomic displacements $\boldsymbol{U}_i$ on $\boldsymbol{Q}$ [66] (for more details, see Appendix B). The quality of the P fits, with Monte Carlo distributed initial parameters, is evaluated by the reduced χ^2 value defined as

$$\chi^2 = \left(\sum_{j=1}^{P} R_j^2\right)/(P-V), \tag{3}$$

where P is the number of data points (number of completed individual fits j) and V is the number of variables.

In the presented paper, the measured RSD spectra above and below T_{CM} have been fitted in two steps. First, the high-temperature P phase has been refined in terms of ADPs and static atomic displacements of the atomic position using the data collected above T_{CM}, then the changes in the static atomic displacements have been reevaluated based on the data measured below T_{CM}.

III. EXPERIMENTAL DETAILS

A. Sample preparation

The YMn_2O_5 crystal (growth described in [67]) has a cuboid shape with an approximate size of $(1 \times 1 \times 2)$ mm. The crystal was oriented with a laboratory single crystal x-ray diffraction machine D8 Quest from Bruker AXS [68]. Due to the spontaneous polarization occurring along the crystal's b axis [21,22], we deposited platinum electrodes onto the {010} faces as electrical contacts. The sample was glued on a sapphire plate, to ensure good thermal conductivity and electrical isolation [69] of the cold head. This sample configuration has been used for the electric characterization as well as for biasing the ferroelectric domains forming upon cooling below T_{CM} (see Sec. III B).

B. Electric characterization of the phase transition temperature

The transition from the P phase to the ferroelectric CM phase (with intermediate ferroelectric phases) induces pyroelectricity as well [33,36,48]. At a macroscopic level, this effect can only be observed if there is a preferred orientation of domains such that the individual current contributions do not cancel each other. Therefore, we cooled the sample in various electric fields to align the domains in the CM phase [70] (more details in Appendix C). The pyroelectric current

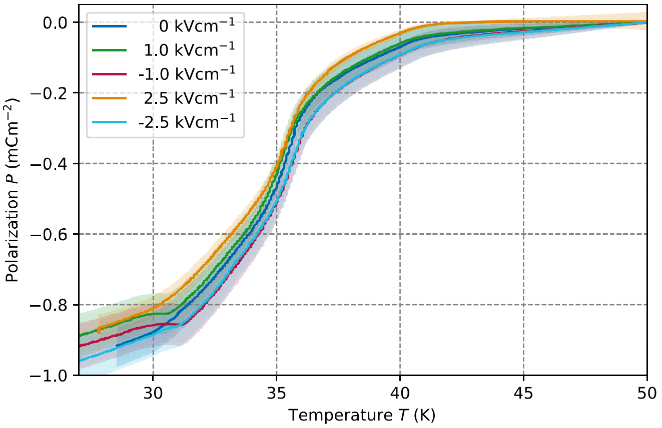

FIG. 4. Temperature-dependent polarization at different electric fields. The lightly colored areas indicate the error level, which mainly originates from the accuracy of the used electrometer. All measured polarizations are similar within the error range. The polarization is equivalently pronounced also without electric field as well as with opposite poling, even above the coercive field strength of 2.2 kVcm^{-1}. An appearance of a measurable polarization below theoretical T_{CM} is clearly visible. We determine the phase transition temperature at $T = (36 \pm 2)$ K.

was integrated over time to obtain the temperature-dependent polarization as shown in Fig. 4. We can clearly identify the transitions from the P to the CM phase [14–16,33] with the appearance of the polarization in the *b* direction. Uncertainties of the temperature reading prevented an accurate investigation of the full temperature dependence of the polarization. Therefore, we could not precisely determine the pyroelectric coefficient or the differential phase transition temperature. The main causes of the uncertainties were the temperature difference between the sensor and the sample, as well as the sensor temperature reading accuracy (±2 K [71]).

The measurements with and without electric field show no differences in the polarization. Thus, the ferroelectric domains have a preferred orientation after cooling down to the CM phase even without external bias, as reported in literature [36,44,48,70], probably due to robust magnetic domains [36,44,72]. No ferroelectric switching of polarization was observed when the sign of the electric field was changed, contradicting in part previous studies [44,48,73]. The absence of ferroelectric switching is not an intrinsic structural property and may be related to structural inhomogeneities and defects, which has been observed before in equivalent crystals and could be removed by annealing the sample [48]. Furthermore, the pyroelectrically measured polarization depends on the history of the domain population [36,44]. The measured polarization without electric field is $P_S = (0.88 \pm 0.06)\ \mathrm{mC\,m}^{-2}$.

C. Synchrotron experiment

RSD measurements were performed during two synchrotron experiments carried out at beamline BM28 (XMaS) [74] of the European Synchrotron Radiation Facility (ESRF) and beamline P23 of the Deutsches Elektronen-Synchrotron (DESY). A different sample holder was designed for each beamline (see Fig. 5). At BM28, we glued the sample with the electrode side directly onto a platinum patch (bottom contact) of a sapphire plate, which served as electric insulation to the cryostat cold finger. The opposite contact was realized using a thin Au wire glued to a second Pt patch on the sapphire plate [Fig. 5(a)]. For the experiment at DESY/P23 we used the same sample setup as for the electrical characterization, explained in detail in Appendix C [Fig. 5(b)].

BM28 was equipped with a six circle Huber diffractometer and a Pilatus3 300K 2D detector. The sample was mounted on a displex cryostat (closed cycle). At beamline P23, a five circle diffractometer, a LAMBDA 2D detector, and a He flow cryostat have been used. We measured energy scans (RSD spectra) for several Bragg reflections close the yttrium absorption edge (tabulated value 17.038 keV [75]). To ensure stable single-phase synchrotron diffraction measurements, we chose to work with sufficient offsets from T_{N_1}, T_{CM}, and T_{N_2}. Therefore, the sample temperature has been set to 50 K and to 30 or 25 K at ESRF/BM28 and DESY/P23, respectively. We applied an electric field of 1.0 kVcm^{-1} during the measurements below T_{CM} to align the ferroelectric domains and thus to facilitate structure analysis.

Due to the large unit cell of $\mathrm{YMn_2O_5}$ and the high photon energy, the Renninger effect [76] of multiple diffraction was a major source of contamination of the data. We performed an azimuthal scan (rotation about the normal of the diffracting lattice plane) for each reflection and at each energy, following the routine of Nentwich *et al.* [77] to eliminate any

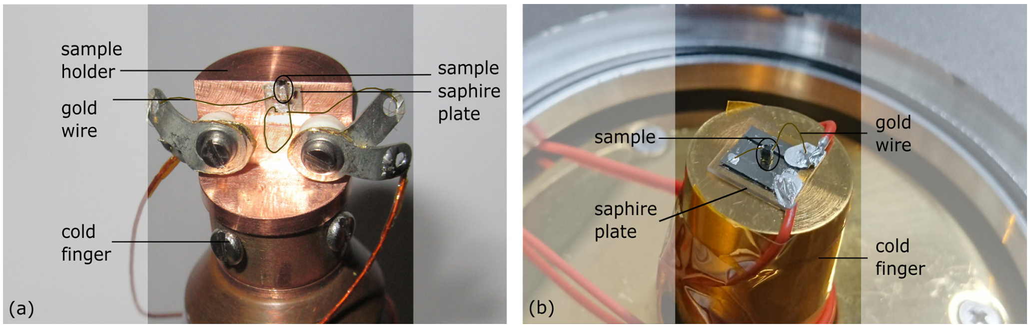

FIG. 5. Electrical setup used for the experiment (a) at beamline BM28 (ESRF) with a closed cycle cryostat and (b) at beamline P23 (DESY) with a He flow cryostat.

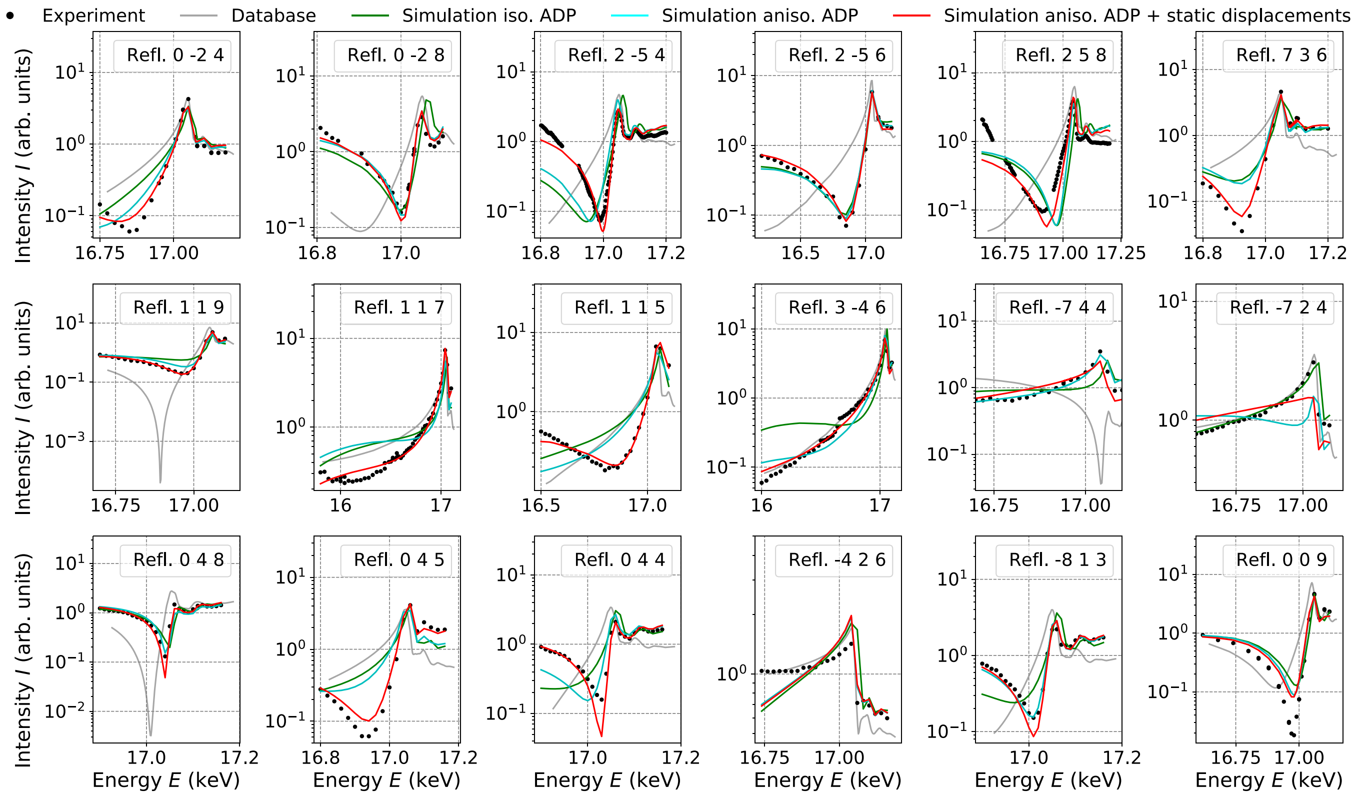

FIG. 6. Experimental and simulated RSD spectra above T_{CM} for selected reflections (Refl.): The initial structure from Kagomiya *et al.* [47] (gray, $\chi^2 = 1.6 \times 10^{-4}$), the best fits using isotropic ADPs (green, $\chi^2 = 5.4 \times 10^{-5}$), those using anisotropic ADPs (cyan, $\chi^2 = 3.8 \times 10^{-5}$), as well as the best fits using anisotropic ADPs and static displacements (red, $\chi^2 = 8.5 \times 10^{-6}$) are shown in comparison.

contributions of the Renninger effect. With this routine, we measured the same reflections for the P and the CM phase.

IV. RESULTS

A. Refinement of the static and dynamic displacement parameters of the P phase

We used the well-known structure of the P phase [47] to determine the static and dynamic displacements in order to obtain a precise reference for the refinement of the CM phase. The results displayed in Fig. 6 show that the structure solutions found in crystallographic databases [47] are not adequate to reproduce the experimental RSD spectra. Given that the static structure of the P phase is well known, the observed deviations between experimental and calculated spectra mainly result from inaccurate values of the ADPs.

The refinement of the structure using the RSD method relies on refining simultaneously the energy dependent intensity of selected reflections (see SM Sec. S I [61]). The spectra of the reflections were computed using the PYTHON package PYASF [78] based on the kinematic theory of diffraction. This is suitable, since the width of the rocking curve from experiment cannot be described with rocking curves simulated using dynamic diffraction theory (see Appendix D), which is caused by the sample mosaicity. In addition, the studied reflections are typically weak so that extinction and other dynamic effects can be neglected. In the refinement, we minimized relative differences of measurement and calculation, which is justified since the errors are dominated by the instrumental stability, e.g., source spectrum, absorption in air and windows, as well as detector efficiency. A detailed description

TABLE I. Results for the anisotropic ADPs at 50 K from the best RSD fit. The errors were calculated from the 3σ level of the reduced χ^2 distribution following [79] (see SM Sec. S II [61]).

Label	U_{11} ($\times 10^{-3}$ Å^2)	U_{22} ($\times 10^{-3}$ Å^2)	U_{33} ($\times 10^{-3}$ Å^2)	U_{12} ($\times 10^{-3}$ Å^2)	U_{13} ($\times 10^{-3}$ Å^2)	U_{23} ($\times 10^{-3}$ Å^2)
Y	0.00(156)	4.37(66)	1.53(77)	−0.99(91)		
Mn1	0.36(111)	3.38(92)	2.44(88)	0.18(91)		
Mn2	2.91(80)	0.00(26)	2.50(90)	−1.29(99)		
O1	2.05(51)	0.52(67)	4.12(117)	−0.88(72)		
O2	0.00(70)	0.31(66)	0.00(20)	−1.52(81)		
O3	1.48(87)	0.27(60)	0.00(86)	0.35(97)		
O4	0.01(44)	0.02(36)	1.97(77)	−1.62(71)	−1.82(68)	−1.51(82)

TABLE II. Refined Wyckoff positions of YMn_2O_5 at 50 K from the results of the best fit in space group *Pbam* (55). Numbers with decimals are free parameters, whereas rational positions are fixed by the site symmetry. Errors result from the 3σ level of the reduced χ^2 distribution following [79] (see SM Sec. S II [61]). Additionally, we added the total displacement *u* from the originally reported structure [47] for each atom.

Label	Wyckoff symbol	*x*	*y*	*z*	*u* (pm)
Y	4*g*	0.1393(4)	0.1665(2)	0	5.3(4)
Mn1	4*f*	0	1/2	0.2544(6)	1.8(5)
Mn2	4*h*	0.397(2)	0.3434(3)	1/2	12.7(13)
O1	4*e*	0	0	0.268(2)	1.7(9)
O2	4*g*	0.085(5)	0.457(2)	0	58.0(40)
O3	4*h*	0.125(3)	0.411(2)	0.5	25.0(30)
O4	8*i*	0.416(2)	0.2061(6)	0.246(3)	15.6(15)

of all the fit parameters is given in Appendix B. To obtain a good agreement between modeled and measured data, we tested different approaches including isotropic or anisotropic ADPs as well as anisotropic ADPs combined without and with small deviations of the atoms' static displacements compared to those obtained in reported crystal structures. In the latter case, we defined fit parameters for all the atomic coordinates that are not restricted by their site symmetry. Figure 6 provides an overview of the data analysis process, showing the initial structure, and the best fits of increasingly complex models with isotropic (green) as well as anisotropic dynamic displacements (cyan), and anisotropic dynamic and static displacements (red). Details about the improvement of the fit procedure and results of the best fits are described in the SM Sec. S II [61].

In the following paragraph, we concentrate on the most complex model, i.e., the one having the largest number of free parameters: anisotropic ADPs with static displacements. Here, we refined 43 structural parameters (13 static and 30 dynamic displacements). The best fit has a reduced χ^2 of 8.5×10^{-6}. All results are physically reasonable and have low error values. Since we fit all reflections simultaneously, the resulting best refinement is a compromise solution for all 18 reflections, which means that a general improvement is accepted even at the expense of a deterioration for one reflection. A further improvement of the model is not possible, since all free structural parameters within the space group were optimized within physically reasonable ranges. Remaining discrepancies between simulation and experiment are due to experimental errors, which are dominated by the crystal shape and mosaicity, the stability of the energy scans, the model for the absorption correction, as well as remaining influences of the Renninger effect after correction. These errors may not be fully captured with the device function, applied filters, and corrections.

Table I lists the ADPs extracted from the best fits. The main differences occur for the positions of the O atoms. The new modeled structure was obtained with a remarkable precision of $\lessapprox$ 4 pm for each Wyckoff position (see Table II). The refined structure of the P phase is illustrated in Fig. 7 (colored balls) and compared with the initial atomic positions (gray balls).

B. Structure refinement of the CM phase

To refine the structure of the CM phase, we investigated differences in the RSD spectra above and below the phase transition (for comparison of both sets of spectra, see Fig. 14 in Appendix E). Here, we are specifically interested in changes of the local intensity minima and their locations on the energy axis, which are particularly sensitive to atomic displacements [50]. These changes of the minima in the spectra are small, but significant. Simulation of the energy-dependent reflections with the refined structure of the P phase does not fit the minimum position very well. Therefore, an adequate structure model needs to be determined. As we know from literature and Sec. III B the spontaneous polarization emerges in the crystallographic *b* direction. The study of the possible subgroups of first and second order revealed that only space group $Pb2_1m$ fulfills the given constraints (polarization in *b* and doubled *c* parameter due to magnetic ordering; see Appendix A) and has been already suggested in literature [21,22,29,46,49]. We used the refinement results from Sec. IV A as initial model and transformed the structural parameters to the $Pb2_1m$ symmetry. In the refinement, we assumed the ADPs and machine function (see Appendix B) as unchanged and only optimized the static displacement parameters, which already count a number of 50 parameters in the CM phase. Figure 8 shows the experimental data at 25 and 30 K, respectively, as well as the reflection intensities

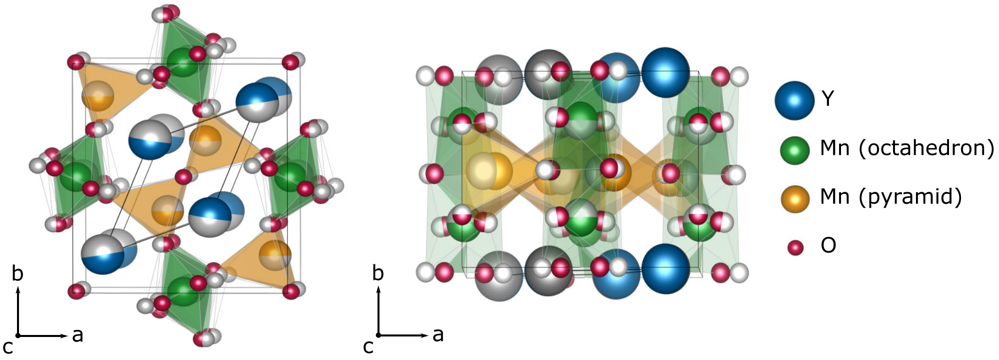

FIG. 7. Visualization of the static atomic displacements based on ICSD No. 165870 [47], before (grayish balls) and after refinement of the P phase (colored balls), in two different projections. The main improvement in the P phase structure concerns the position of the oxygen atom.

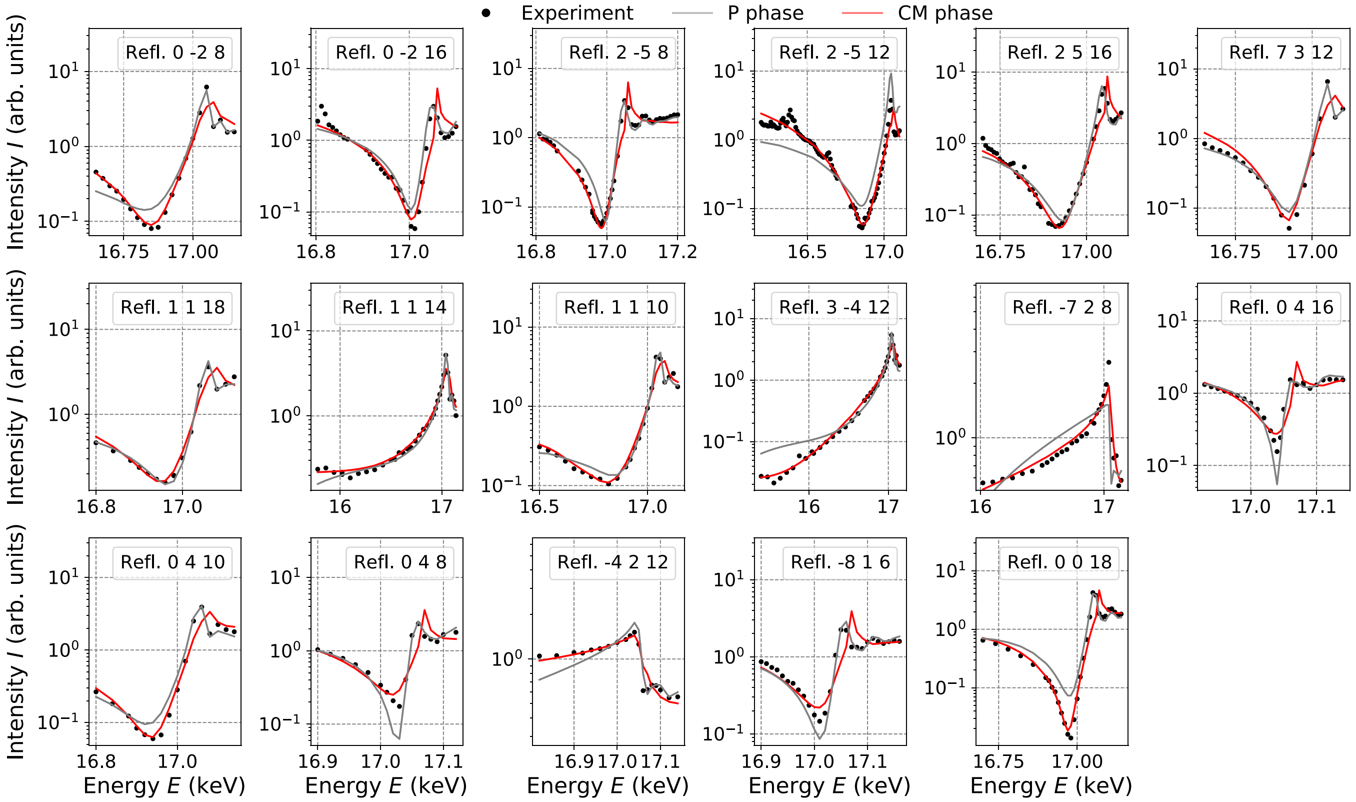

FIG. 8. Simulation of RSD spectra of the refined CM phase (red) in comparison to the best refinement of the P phase (gray), as well as the experimental data below the phase transition temperature. With the additional degrees of freedom in space group $Pb2_1m$ the reduced χ^2 has improved to 1.96×10^{-5} from 3.3×10^{-4} for the unrefined parameters from the P phase. The simulated RSD spectra of the CM phase show in particular an improved concordance with the most sensitive region of the intensity minimum.

simulated with the refinement results of the P phase (gray) and the CM phase (red). The additional structural degrees of freedom of the CM phase significantly improve the simulated spectra in contrast to the high-symmetry restricted spectra. The reduced χ^2 improves from 3.3×10^{-4} to 1.96×10^{-5}.

The results of the refined static atomic displacements are listed in Table III and respective shifts are visualized compared to static displacements of the P phase in Fig. 9. Again, in terms of precision and within the made assumptions, remarkably small errors (for each coordinate on a Wyckoff site) in the order of $\lessapprox 6$ pm for Y and Mn as well as $\lessapprox 38$ pm for the O are reached by the RSD method. It should be noted that uncertainties for ions with a lower number of electrons, in this case the oxygen partial structure, are greater due to the chosen x-ray probe. The structural changes induced by the phase transition from P to CM phase incorporate total displacements u in the order of 5 to 58 pm. The shift of u_y in the negative direction for Mn and in the positive direction for O within the asymmetric unit along the y direction directly contributes to the polarization along the b direction.

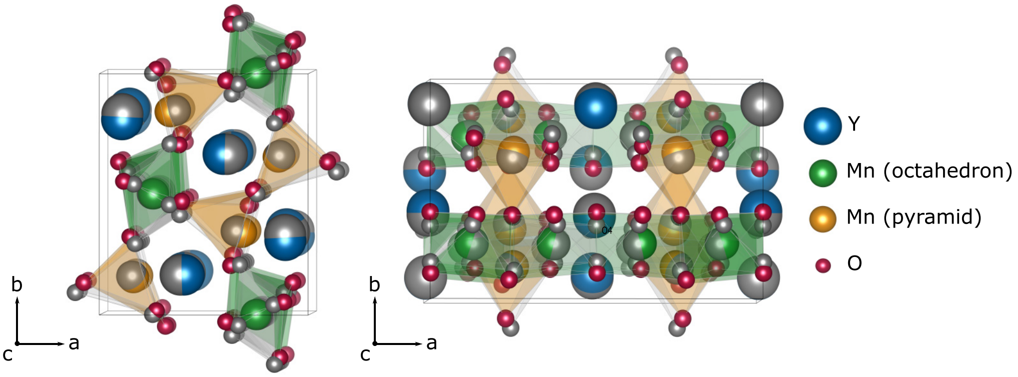

FIG. 9. Visualization of the static atomic displacements (colored balls) of the CM phase in comparison to those of the P phase (gray) in two different projections. Remarkable is in particular the most prominent movement of Mn^{3+} ions outside of the pyramid's basal plane.

TABLE III. Refined Wyckoff positions of the CM phase of YMn_2O_5 from the results of the best fit in space group $Pb2_1m$ (26). The first index of the label refers to the label used in the higher symmetric space group *Pbam* (55) (see Table II). Numbers with decimals are free parameters, whereas rational positions are fixed by the site symmetry. Errors result from the 3σ level of the reduced χ^2 distribution following [79] (see SM Sec. S III [61]). Furthermore, we present the additional static shifts u_y in the y direction and the total additional displacement u in comparison to the P phase for each atom within the asymmetric unit.

Label	Wyckoff symbol	x	y	z	u_y (pm)	u (pm)
Y11	2*a*	0.405(4)	0.167(3)	0	1(2)	11(3)
Y12	2*a*	0.109(5)	0.810(4)	0	−10(4)	20(4)
Y21	2*b*	0.382(4)	1/6	1/2	0	5(3)
Y22	2*b*	0.123(4)	0.848(8)	1/2	12(6)	15(6)
Mn11	4*c*	0.253(5)	1/2	0.121(2)	0	5(3)
Mn12	4*c*	0.252(5)	0.500(4)	0.632(2)	−1(3)	6(3)
Mn21	4*c*	0.330(4)	0.839(2)	0.254(3)	−4(2)	18(3)
Mn22	4*c*	0.153(5)	0.151(2)	0.255(4)	−5(2)	7(15)
O11	4*c*	0.27(5)	0.02(4)	0.131(7)	14(37)	18(4)
O12	4*c*	0.30(5)	0.95(4)	0.639(7)	−45(38)	58(14)
O21	2*a*	0.39(2)	0.472(9)	0	13(8)	41(15)
O22	2*a*	0.12(3)	0.55(3)	0	10(26)	35(13)
O23	2*b*	0.39(2)	0.472(9)	1/2	13(8)	41(15)
O24	2*b*	0.12(2)	0.55(3)	1/2	10(26)	33(16)
O31	4*c*	0.38(1)	0.46(1)	0.246(4)	39(9)	42(9)
O32	4*c*	0.08(2)	0.63(2)	0.23(1)	35(16)	53(16)
O41	4*c*	0.376(2)	0.70(2)	0.135(3)	−3(15)	35(3)
O42	4*c*	0.14(1)	0.32(2)	0.137(1)	24(15)	33(13)
O43	4*c*	0.38(2)	0.74(2)	0.367(3)	30(16)	46(16)
O44	4*c*	0.14(1)	0.31(2)	0.363(1)	17(15)	28(11)

V. DISCUSSION

A. Results of the refinement of the P phase

As shown in Sec. IV A, we refined the structure of YMn_2O_5 in the P phase at 50 K with RSD and obtained small but substantial differences in atomic positions with respect to the structure solution from [47], especially for the oxygen partial structure with a maximum static displacement of 58 pm, next to significantly improved values for the ADPs. The general sensitivity of the RSD method to displacements, estimated by means of the uncertainties in the structure solution of the P phase, can be specified with a range between 0.4 and 4 pm with an average of 1.7 pm. This corresponds to the sensitivity of the RSD method, as already found in [50].

The agreement between simulation and experiment has been gradually enhanced by increasing the complexity of the underlying structure models, starting from database entries and isotropic ADPs and reaching up to anisotropic ADPs with completely uncoupled static displacements. These improvements are clearly documented in the reduction of χ^2 by a factor of 20 (see SM Sec. S II [61]). In order to verify the stability of the obtained fit results and identify correlations (SM Sec. S II [61]), we explored the parameter space by repeating the fit with Monte Carlo distributed initial parameters while keeping selected parameters fixed within a certain predefined range. To get dense projections for each fit parameter, we performed about 10^7–10^8 individual fits on the TUBAF HPC cluster (≈350 TFlops^{-1} CPU). Most of the parameters show no interdependencies with other parameters, only a few correlations and respective increase in the error envelopes have been found within the experimental data (see SM Sec. S II [61]). Since the initial structure is known within the 1 Å resolution of conventional x-ray diffraction techniques [80,81], we restrict the parameter space of the static displacements within limits up to this value. In consequence, all fit parameters converge in a stable global minimum. The electric measurement shows no polarization above T_{CM} and therefore no hint of ferroelectricity in the P phase and the nonpolar space group *Pm* as Balédent *et al.* suggested for other Mn-based mullites [82].

B. Results of the refinement of the CM phase

Due to the high sensitivity of the RSD method to displacements partly in the subpicometer range, we were able to refine the structure of the CM phase and can give its first structure solution in space group $Pb2_1m$ with $Z = 8$ formula per units in a $1 \times 1 \times 2$ supercell with respect to the initial structure and with lattice parameters $a = 7.244$ Å, $b = 8.463$ Å, and $c = 11.314$ Å (Fig. 9). Again, we performed about 10^7 individual fits to get a significant statistical coverage within the parameter space for all 50 fit parameters in well-defined ranges with physical reasonable limits of ±0.06 for all positional degrees of freedom (in fractional coordinates). To prevent a positional phase drift of the whole structure in the polar direction, we fixed one atom at the origin for all fits. Additionally, we again varied the initial parameters randomly and kept two randomly selected parameters fixed during an individual fit to probe the development of the reduced χ^2 in parameter space and to reveal parameter correlations. Since no additional Bragg reflections could be observed for the CM phase and changes in the RSD spectra are minuscule (see Fig. 14), we expected only slight additional displacements during the phase transition. Thus, we further restricted the limits in parameter space to below ±0.7 Å. As a result, most parameters converge to a stable global minimum in the reduced χ^2 space, but in particular the parameters of a displacement in the doubled z direction show two minima. However, no significant discrete or linear correlations between the parameters with two minima, as well as with other parameters, could be found (see SM Sec. S III [61]). Rather, the respective correlations show a pronounced fourfold symmetric-antisymmetric X shape (Fig. S11 in SM Sec. S III [61]). This may be an indication for disorder in the average structure rather than for two or more classes of separate possible structure solutions. Additionally, we checked the uniqueness of our structural model for the five best fit results. All models are equal within the error range (see SM Sec. S III [61]). It should be noted that experimental errors (see Sec. IV A) which are not captured by the P phase refinement will also affect the CM phase results. These errors could be further reduced by an optimized setup for temperature or field and wavelength dependent measurements for low resolution x-ray diffraction. The future of the technique will be a combination with full Ewald sphere (state-of-the-art resolution) single crystal diffraction, potentially allowing thousands of reflections to be measured.

The refinement shows a significant movement of the ions due to the phase transition, with the largest shifts being present within the O partial structure exhibiting a maximum of $u = 58\,\mathrm{pm}$ in the pyramid. The Mn atoms centering pyramids have a strong movement of up to 18 pm along the pyramidal axis, whereas Mn inside the octahedra only moves about 6 pm. Remarkably, without predefined tendency within the fit routine, the refined static displacements show an opposite movement of the positively charged $\mathrm{Mn}^{3+}/\mathrm{Mn}^{4+}$ and the negatively charged O^{2-} partial structure, complying with the expected anionic/cationic movement given by the direction of the external electric field (see u_y in Table III). Uncertainties in the total additional displacement u in the structure solution of the CM phase can be specified in a range between 3 and 16 pm with an average of 10.1 pm.

The refined crystallographic space group $Pb2_1m$ corresponds well with the findings from the investigation of the magnetic structure with neutron diffraction [83], where the magnetic point group is refined with $m2m$ [23,44,46] allowing a polarization in the b direction, as well as with magnetoelectric measurements [46]. The results of the present paper are applicable, for all isostructural Mn-based mullites, which shows similar electric and magnetic behavior and where $Pb2_1m$ has been already discussed as a possible space group [22,33,36,83–90].

C. Origin of ferroelectricity in the CM phase

By means of the RSD method, we finally discovered the atomistic origin of the ferroelectricity in the CM phase. As described in Sec. V B, the movement of the ions, especially of Mn and O partial structure, obeys the development of an oriented dipolar structure. The spontaneous polarization P_S, induced by this ionic movement, can be estimated with an approach outlined by Weigel *et al.* [91], based on considerations of Peng *et al.* [92] and the "modern theory of polarization" by Resta [93], King-Smith *et al.* [94], and Vanderbilt *et al.* [95].

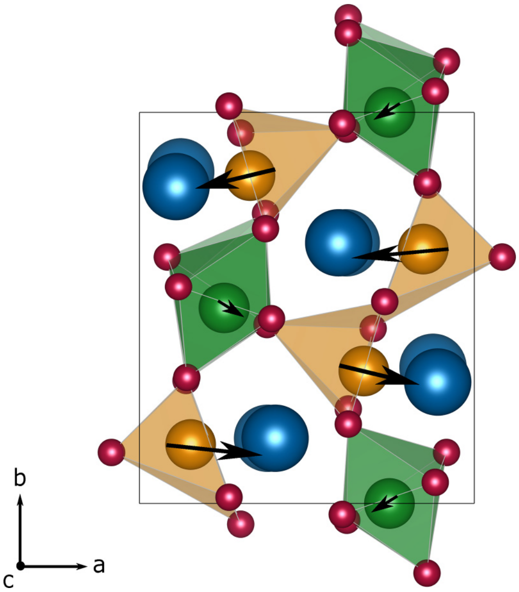

FIG. 10. The resulting polarization in the CM phase of $\mathrm{YMn_2O_5}$ due to structural displacements is visualized exemplarily by the Mn vectorial contributions (black arrows). The main contribution originates in particular from the displacement of the Mn^{3+} ions with respect to the surrounding O pyramid.

The approach employs the positional shifts $u_{j,l}$ between P and CM phase in direction l from the experimental data for each atom j as well as the *Born effective charges* (BECs) $Z^*_{j,kl}$ computed by first-principle methods (for details in Appendix F). P_S in direction k can be calculated as

$$P_{S,k} = \frac{e}{V_{\mathrm{UC}}} \sum_{j=1}^{N} Z^*_{j,kl} u_{j,l}. \tag{4}$$

with the elementary charge e, the unit cell volume V_{UC}, and the number of atoms in the unit cell N. Here, we calculated an absolute spontaneous polarization of $P_S = (1.3 \pm 0.4)\,\mathrm{mC\,m^{-2}}$ in the b direction from the experimental data. This value is in good agreement with the measured polarization $P_S = (0.88 \pm 0.06)\,\mathrm{mC\,m^{-2}}$ and with experimental polarization reported in literature of around $1.0\,\mathrm{mC\,m^{-2}}$ [46,70]. The calculated P_S has the strongest contribution from the pyramids and smaller parts from the octahedra. Figure 10 visualizes the vectorial contributions from the Mn partial structure, which directly reflects the atomistic movement due to the phase transition. These findings match postulations in literature [24,34,46], which state that the displacement of the Mn^{3+} ions in the pyramids (total Mn^{3+} contribution $P_S \approx 0.04\,\mathrm{mC\,m^{-2}}$) is more important for the manifestation of ferroelectricity than that of Mn^{4+} ions in the octahedra (total Mn^{4+} contribution $P_S \approx 0.005\,\mathrm{mC\,m^{-2}}$). Additionally, we can confirm that Y is displaced [48], giving further contributions to the polarization, where the individual contributions partially compensate each other to a total $P_S \approx 0.01\,\mathrm{mC\,m^{-2}}$. The remaining part of P_S is due to the substantial shift in O partial structure, especially the flexible movement of the oxygen position of the pyramid top, corner sharing with the octahedron.

As has been summarized, the literature controversially discusses several mechanisms for magnetically driven ferroelectricity: symmetric exchange ($P_{S,\mathrm{SE}} \propto \boldsymbol{S}_i \cdot \boldsymbol{S}_j$, with $\boldsymbol{S}$ the spin of the magnetically active ions i and j) or antisymmetric inverse Dzyaloshinskii-Moriya interaction ($P_{S,\mathrm{DM}} \propto \boldsymbol{S}_i \times \boldsymbol{S}_j$) [15,28]. For comparison, we calculated $P_{S,\mathrm{SE}} \approx 0.74\,\mathrm{mCm}^{-2}$ and $P_{S,\mathrm{DM}} \approx -0.08\,\mathrm{mCm}^{-2}$ with the magnetic moments from Kim *et al.* [39]. The findings support in particular those results that favor the contribution of both components to the polarization, but evidently the symmetric exchange interaction is predominant [24,27,28,44]. Thus, magnetostriction due to symmetric exchange interactions shifts ions to optimize the spin-exchange energy [21,23,24,34].

In addition, our results confirm that the polarization in the CM phase does not exclusively have an electronic contribution $P_{S,\mathrm{El}}$ due to spin-dependent hybridizations of O and Mn orbitals [49,96], but also has an ionic contribution $P_{S,\mathrm{Ion}}$ induced by shifts of the ions due to the phase transition. Furthermore, P_S calculated from structural parameters shows a better agreement with the experimental values than an estimation of P_S based on spin interactions. The results are of high interest for all material systems, where a strong coupling between electric and magnetic properties exists [97–102].

VI. CONCLUSION

We investigated the origin of ferroelectricity of the CM phase in $\mathrm{YMn_2O_5}$ using the resonant x-ray diffraction method called RSD with a sensitivity to atomic displacements in the picometer range. We started with the refinement of dynamic and static atomic displacements of the P phase above T_{CM} to receive a highly precise structure model as a basis for structural changes during the phase transition to the CM phase. We significantly improved the structure solutions of the P phase in space group *Pbam* found in crystallographic databases. For the refinement of the P phase we had in total 43 structural degrees of freedom, which converged to a stable minimum. We used the refined P phase as initial model for the refinement of the CM phase and optimized 50 static displacement parameters in space group $Pb2_1m$. With the superior confidence levels in the lowered symmetry, we present the first structural model of the CM phase in $\mathrm{YMn_2O_5}$.

Next to providing insights to the structural subtleties of the P as well as of the CM phase of $\mathrm{YMn_2O_5}$, we have shown that the new RSD method is capable of refining structures with more than 50 structural degrees of freedom (for the CM phase, 30 ADPs and 13 static displacements for the P phase), based on RSD spectra of 18 reflections (compared to four free structural parameters in our first application of the method for polar $\mathrm{SrTiO_3}$). The methodical advancements in this paper comprise the significantly increased number of structural degrees of freedom for the $\mathrm{YMn_2O_5}$ structure solutions and an improved iterative algorithm for the identification of relevant reflections (see SM Secs. S I and S II [61]).

The investigations of the RSD spectra below T_{CM} show significant displacements of the ions, especially a shift of O and Mn partial structure in opposite directions. Here, the displacement of Mn^{3+} within the pyramid has a strong contribution to the ferroelectricity. The presented findings give an answer to the origin of ferroelectricity in $\mathrm{YMn_2O_5}$ as well as confirm structural predictions and suggestions from literature. The physical mechanism behind the ferroelectricity is magnetostriction, which shifts ions to optimize the exchange interactions. These shifts are very small, but with the high spatial resolution of RSD, we were finally able to experimentally determine the atomistic displacements and confirm an ionic contribution to the spontaneous electric polarization. The presented results are interesting for all isostructural Mn-based mullites and materials with strong coupling between magnetic and electric properties.

ACKNOWLEDGMENTS

Financial support is cordially acknowledged from Deutsche Forschungsgemeinschaft (REXSuppress Grant No. 324641898 and AcoustREXS Grant No. 409743569) and from the European Union research and innovation program Horizon 2020 EURIZON (formerly CREMLINplus 871072). We acknowledge the European Synchrotron Radiation Facility for provision of synchrotron radiation facilities (Proposal No. MA 3817) and we would like to acknowledge assistance and support in using beamline BM28. Additionally, we acknowledge DESY (Hamburg, Germany), a member of the Helmholtz Association HGF, for the provision of experimental facilities. Parts of this research were carried out at PETRA III using beamline P23. Beamtime was allocated for Proposal No. I-20190565. Furthermore, we acknowledge the Compute Cluster 2019 of the Faculty of Mathematics and Computer Science of Technische Universität Bergakademie Freiberg, operated by the computing center (URZ) and funded by the Deutsche Forschungsgemeinschaft (Grant No. 397252409) for provision of high performance computing.

APPENDIX A: DETERMINING SUBGROUPS OF *Pbam* WITH DOUBLED *c* AXIS AND POLARIZATION ALONG *b*

The solid basis of a reliable structure refinement is the correct choice of space group. For the low-temperature CM phase, we are searching for a subgroup of *Pbam* with doubled c axis and polarization along the b direction (with respect to the settings of *Pbam*). The structured investigation started by listing all symmetry transitions involving two steps with respect to maximal subgroups as listed in the International Tables [103]. The resulting Bärnighausen-like tree in Fig. 11 also displays the affiliation of the space group to a polar or nonpolar point group (blue and red box color, respectively). Further, the permutation and potential multiplication of the lattice vectors is presented; invalid values are highlighted in red. In summary, all space groups are crossed out that are nonpolar or that do not represent a permutation of the lattice vectors a, b, and $2c$.

Subsequently, the resulting space groups were studied in more detail. Now, we compared the polarization axis of the space group to the lattice vectors (with respect to space group *Pbam*). This flock of space groups has orthorhombic or lower symmetry, thus each position of the Hermann-Mauguin nomenclature stands for a crystallographic lattice vector. Here, the rotation or screw axis corresponds to the polar axis. Hence, we can exclude all space groups where the rotation or

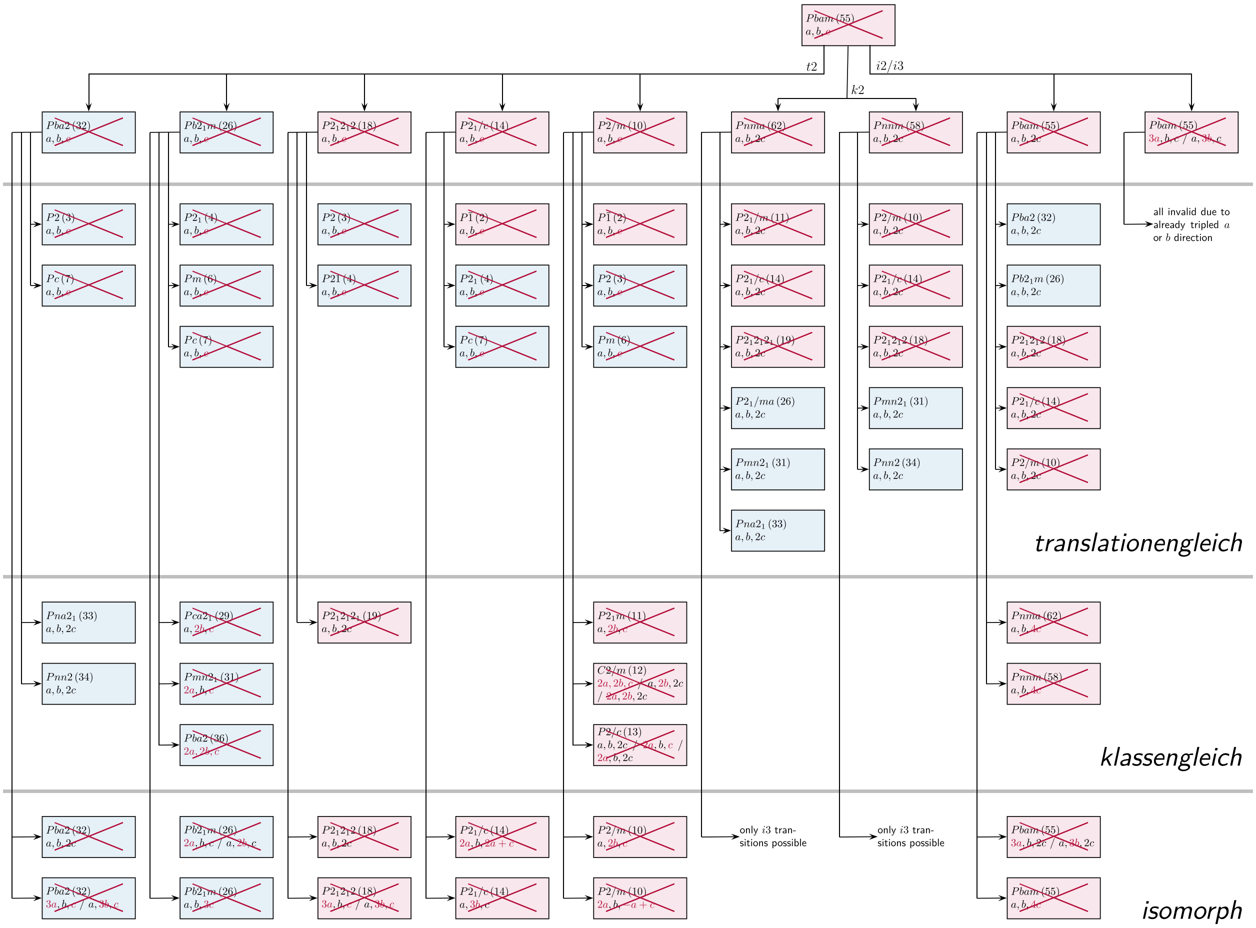

FIG. 11. Bärnighausen-like tree of YMO with space group *Pbam* (55). The diagram shows the symmetry transitions involving two steps with respect to maximal subgroups (translationsgleich, klassengleich, and isomorph) as listed and labeled in the International Tables [103]. In addition to the space group name, the boxes list the permutation and multiplicity of the lattice vectors. Inappropriate multiplicities are marked in red. The background color of the box shows whether the corresponding point group is polar (blue) or nonpolar (red). In total, all those space groups are crossed out that are nonpolar or have a wrong multiplicity of the lattice vectors.

screw axis does not coincide with the b vector of *Pbam*. As a result, only $Pb2_1m$ (26), $a\,b\,2c$ and $Pmn2_1$ (31), $2c\,a\,b$ are valid space groups with respect to the considered conditions. Please note that $Pb2_1m$ (26), $a\,b\,2c$ and $Pmc2_1$ (26), $2c\ -b\,a$ as well as $Pmn2_1$ (31), $2c\,a\,b$ and $P2_1nm$ (31), $a\,b\,2c$ are not isostructural.

In the structurally related $BiMnO_5$, the polarization change and doubling in the c direction is attributed to the relative displacement between the O and Mn ions, not between O and Bi [104]. These displacements are only allowed for space group 26, therefore, we can exclude space group 31 from further considerations.

APPENDIX B: DETAILS OF THE FIT ROUTINE

To determine the structure factor $F(E, \boldsymbol{Q})$ according to Eq. (2), the nonresonant atomic scattering factors $f_{i,0}(\boldsymbol{Q})$ were taken from the International Tables of Crystallography C [105]. The resonant part of the scattering factors results from the absorbing atom, which we measured during our experiments. The near-edge fine structure in $f_i'(E)$ and $f_i''(E)$ for Y was obtained with x-ray absorption spectroscopy data of YMn_2O_5 powder measured at the Y absorption edge and

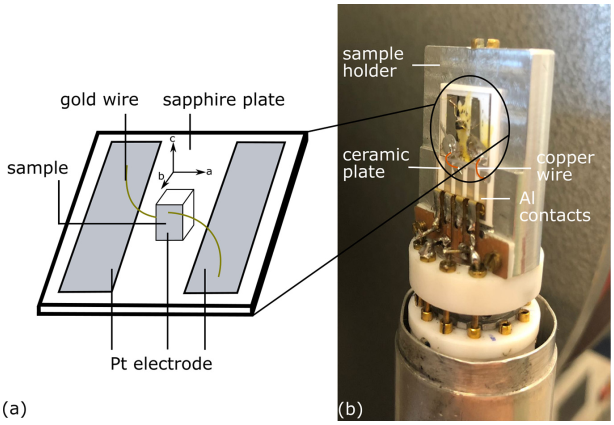

FIG. 12. (a) Schematic of the sample setup. The sample is mounted on an electrically insulating sapphire plate and aligned such that an electric field is applied in the b direction (the coordinate system marks the sample orientation). (b) The entire sample holder mounted at the end of the cold finger of the cryostat for electric characterization. The sapphire was placed onto a ceramic plate and the electrodes on sapphire have been connected to the sample holder by copper wires to the circuit leading outside the cryostat.

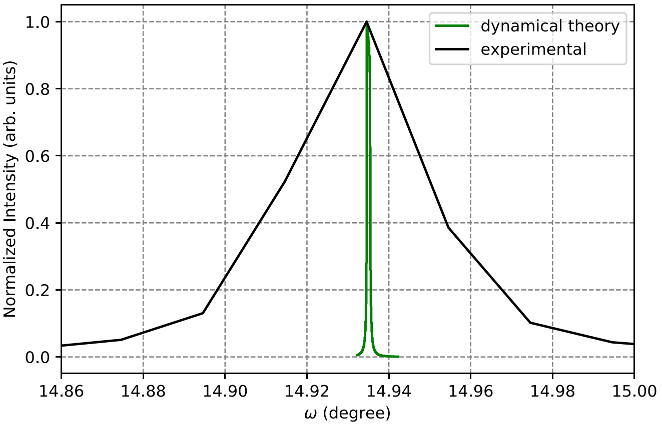

FIG. 13. Calculation of the rocking curve of the 004 reflection with dynamical theory (green) in comparison to experimental data (black). The diffraction data reflect a mosaic crystal.

by application of the Kramers-Kronig relation [106,107]. Furthermore, the dispersion terms f_i' and f_i'' far off the edge have been taken from the Sasaki database [108]. All atomic sites are considered fully occupied.

Further fit parameters comprise a linear device function, which we multiplied to Eq. (1) for each reflection, as well as an energy error and constant background depending on the used beamline. As the spectra are normalized to their mean value, the device function only consists of a slope m to consider spectral drift due to different energy dependencies in the experimental setup, e.g., source spectrum, absorption in air and windows, as well as detector efficiency. This slope is fairly identical for each reflection measured during the same beamtime. With this slope and a beamtime-dependent constant background we can compensate discrepancies in the setup between the two beamtimes. The energy shift corrects small deviations of the absorption edge from the database value induced by inaccuracies of the monochromator and/or undulator positions.

To receive physically reasonable ADPs (small values at low temperatures) for the P phase, we added a minor quadratic penalty function, which punishes unphysically high or low values. Typical ADP values are in the range of 0.005 to 0.02 Å^2 for heavy atoms as well as 0.02 to 0.2 Å^2 for light and strong vibrating atoms [109]. To explore the development of the cost function away from the local minima of the fit, we fixed two randomly chosen fit parameters.

APPENDIX C: ELECTRICAL CHARACTERIZATION

The experimental setup for the electric characterization is shown in Fig. 12. A closed cycle He cryostat was used to cool the sample down to 27 K, i.e., below the phase transition temperature of 39 K. Given the small sample size, a well-defined pyroelectric current signal requires temperature change rates in the order of Kelvin per second [110]. The employed cryostat facilitates these rates only during heating up. Thus, we adapted the measurement strategy of

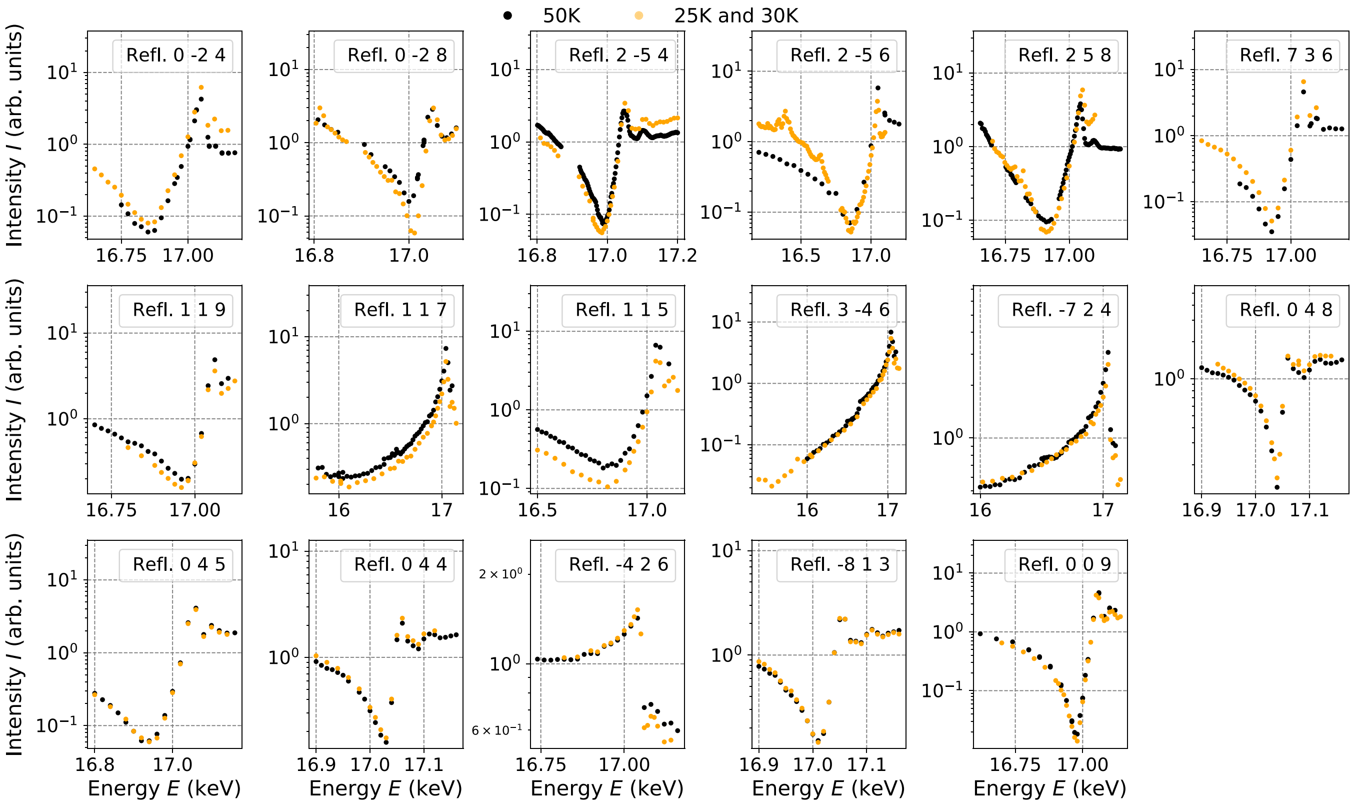

FIG. 14. Comparison of the RSD spectra measured at 50 K (black) and 30 or 25 K (orange). The energy dependencies above and below the phase transition change only slightly.

TABLE IV. BEC tensor given explicitly for the asymmetric units in GS at $T = 0$ K for YMn_2O_5 in the supercell of the CM phase.

Label	x	y	z	Label	x	y	z
Y11	4.39056	−0.61531	0.00000	Y12	4.39056	−0.61531	0.00000
	−0.06883	3.82374	0.00000		−0.06883	3.82374	0.00000
	0.00000	0.00000	5.45163		0.00000	0.00000	5.45163
Y21	4.39056	−0.61531	0.00000	Y22	4.39056	−0.61531	0.00000
	−0.06883	3.82374	0.00000		−0.06883	3.82374	0.00000
	0.00000	0.00000	5.45163		0.00000	0.00000	5.45163
Mn11	2.89881	2.79633	0.00000	Mn12	2.89881	2.79633	0.00000
	1.50323	4.75270	0.00000		1.50323	4.75270	0.00000
	0.00000	0.00000	−2.59602		0.00000	0.00000	−2.59602
Mn21	−1.50810	−0.70330	0.00000	Mn22	−1.50810	0.70330	0.00000
	0.05365	4.05854	0.00000		−0.05365	4.05854	0.00000
	0.00000	0.00000	3.01247		0.00000	0.00000	3.01247
O11	−1.60461	1.32955	0.00000	O12	−1.60461	1.32955	0.00000
	0.01428	−2.59092	0.00000		0.01428	−2.59092	0.00000
	−0.00000	0.00000	−2.02201		0.00000	0.00000	−2.02201
O21	−1.07083	−0.65993	0.00000	O22	−1.07083	0.65993	0.00000
	−0.30513	−2.23265	0.00000		0.30513	−2.23265	0.00000
	0.00000	0.00000	−5.91868		0.00000	0.00000	−5.91868
O23	−1.07083	−0.65993	0.00000	O24	−1.07083	0.65993	0.00000
	−0.30513	−2.23265	0.00000		0.30513	−2.23265	0.00000
	0.00000	0.00000	−5.91868		0.00000	0.00000	−5.91868
O31	−0.01194	−0.36431	0.00000	O32	−0.01194	−0.36431	0.00000
	0.18638	−1.15306	0.00000		0.18638	−1.15306	0.00000
	0.00000	0.00000	4.63108		0.00000	0.00000	4.63108
O41	−1.54695	1.40521	0.72939	O42	−1.54695	−1.40521	0.72939
	0.47886	−3.32917	−0.81772		−0.47886	−3.32917	0.81772
	−0.43506	0.64323	−1.27923		−0.43506	−0.64323	−1.27923
O43	−1.54695	1.40521	−0.72939	O44	−1.54695	−1.40521	−0.72939
	0.47886	−3.32917	0.81772		−0.47886	−3.32917	−0.81772
	0.43506	−0.64323	−1.27923		0.43506	0.64323	−1.27923

Chaudhury *et al.* [70]: aligning the domains during cooling with an applied electric field, removing the field, heating the sample by switching off the cooling system, and then measuring the pyroelectric current during heating with a Keithley 617 electrometer. The transient temperature change of the sample is well reproducible; however, the rate of temperature change is not constant.

To check if a ferroelectric switching of the polarization can be enforced, we studied the polarization saturation while cooling the sample. We applied electric fields below and above the coercive field strength of 2.2 $\mathrm{kV\,cm^{-1}}$ [44] (±1.0 and ±2.5 $\mathrm{kV\,cm^{-1}}$) and made an additional measurement in zero field.

APPENDIX D: SIMULATION OF ROCKING CURVES WITH DYNAMICAL THEORY

The simulation of the RSD spectra with PYASF [78] is based on the kinematical theory of diffraction. To confirm that dynamical effects can be neglected, we compare the measured Bragg peak width with dynamical simulations for the 004 reflection. During the experiment, we measured rocking curves (variation of the Bragg angle ω, fixed detector position 2θ) at 17 keV to acquire integrated intensities as diffraction data. We simulated the rocking curve of the 004 reflection for the same energy, corrected for an energy shift of 28 eV for the reflections measured at DESY extracted from the refinement of the RSD spectra (see Sec. III C). The comparison between experimental and simulated data in Fig. 13 clearly shows that the shape of the rocking curve cannot be described by the dynamical theory, which means that the sample is an imperfect, real mosaic crystal. For this reason, the simulation of the RSD spectra based on the kinematic theory is adequate.

APPENDIX E: COMPARISON OF RSD SPECTRA BELOW AND ABOVE PHASE TRANSITION TEMPERATURE

We investigate the possibility to resolve the minuscule polar displacements, as predicted in literature for the P to CM phase transition, by means of RSD. Figure 14 shows the RSD spectra at 50 K (black) and 30 or 25 K (orange) in comparison. The energy dependencies only change slightly, but the differences are sufficient for a structural refinement by means of the RSD method.

APPENDIX F: CALCULATION OF THE POLARIZATION FROM STRUCTURAL CHANGES

To compute the BEC tensors, a *density functional theory* relaxed structure in ground state ($T = 0$ K) is necessary.

The density functional theory calculation of the structure of YMn_2O_5 was performed with the *ab initio* simulation software VASP and the projector-augmented wave method [111]. Generalized gradient approximation was chosen in Perdew-Burke-Ernzerhof parametrization [112] to account for the exchange-correlation functional. The total energies converged within 10^{-7} eV with a maximum kinetic energy of 450 eV for the basis of the plane waves and the Γ point centered in a $8 \times 6 \times 10$ k-point mesh according to Monkhorst and Pack [113]. The sampling of this mesh is finer than $0.02 \times 2\pi\,\text{Å}^{-1}$. Atom positions and cell parameters were completely relaxed in the chosen space group *Pbam* with residual forces less than 10^{-4} eVÅ^{-1}. In the following, the BEC tensors have been computed by means of *density functional perturbation theory* as implemented in the VASP code. The convergence criterion was set to 10^{-9} eV to obtain highly precise BEC. We computed the tensors for the P phase in space group *Pbam* and transformed the tensors to the supercell of the CM phase for the calculation of P_S with Eq. (4). The calculated BEC tensors are listed in Table IV. Subsequently, we multiplied the tensors with the experimentally determined atomic displacement vectors to compute the electric polarization.

---

[1] I. H. Lone, J. Aslam, N. R. E. Radwan, A. H. Bashal, A. F. A. Ajlouni, and A. Akhter, Multiferroic ABO_3 transition metal oxides: A rare interaction of ferroelectricity and magnetism, Nanoscale Res. Lett. **14**, 142 (2019).

[2] M. Gajek, M. Bibes, S. Fusil, K. Bouzehouane, J. Fontcuberta, A. Barthelemy, and A. Fert, Tunnel junctions with multiferroic barriers, Nat. Mater. **6**, 296 (2007).

[3] E. Lage, N. Urs, V. Röbisch, I. Teliban, R. Knöchel, D. Meyners, J. McCord, and E. Quandt, Magnetic domain control and voltage response of exchange biased magnetoelectric composites, Appl. Phys. Lett. **104**, 132405 (2014).

[4] A. S. Tatarenko, G. Srinivasan, and M. I. Bichurin, Magnetoelectric microwave phase shifter, Appl. Phys. Lett. **88**, 183507 (2006).

[5] T.-D. Onuta, Y. Wang, C. J. Long, and I. Takeuchi, Energy harvesting properties of all-thin-film multiferroic cantilevers, Appl. Phys. Lett. **99**, 203506 (2011).

[6] D. Khomskii, Classifying multiferroics: Mechanisms and effects, Physics **2**, 20 (2009).

[7] H. Schneider and S. Komarneni, *Mullite* (Wiley, New York, 2005).

[8] K. Momma and F. Izumi, Vesta 3 for three-dimensional visualization of crystal, volumetric and morphology data, J. Appl. Crystallogr. **44**, 1272 (2011).

[9] F. Wunderlich, T. Leisegang, T. Weißbach, M. Zschornak, H. Stöcker, J. Dshemuchadse, A. Lubk, T. Führlich, E. Welter, D. Souptel, S. Gemming, G. Seifert, and D. C. Meyer, EXAFS, XANES, and DFT study of the mixed-valence compound YMn_2O_5: Site-selective substitution of Fe for Mn, Phys. Rev. B **82**, 014409 (2010).

[10] X. Wan, L. Wang, S. Zhang, H. Shi, J. Niu, G. Wang, W. Li, D. Chen, H. Zhang, X. Zhou, and W. Wang, Ozone decomposition below room temperature using mn-based mullite YMn_2O_5, Environ. Sci. Technol. **56**, 8746 (2022).

[11] K. M. Alam, S. Gusarov, M. Supur, P. Kumar, A. E. Kobryn, K. Cui, R. L. McCreery, and K. Shankar, Hot hole transfer from Ag nanoparticles to multiferroic YMn_2O_5 nanowires enables superior photocatalytic activity, J. Mater. Chem. C **10**, 4128 (2022).

[12] X. Mu, W. Wang, K. Zhang, H. Ding, and W. Pan, Promoted catalytic properties of acetone over cerium-modified mullite catalyst YMn_2O_5, Aerosol and Air Quality Research **23**, 220302 (2023).

[13] R. A. de Souza, U. Staub, V. Scagnoli, M. Garganourakis, Y. Bodenthin, S.-W. Huang, M. García-Fernández, S. Ji, S.-H. Lee, S. Park, and S.-W. Cheong, Magnetic structure and electric field effects in multiferroic YMn_2O_5, Phys. Rev. B **84**, 104416 (2011).

[14] I. Kagomiya, H. Kimura, Y. Noda, and K. Kohn, Incommensurate antiferromagnetic ordering of ferroelectric YMn_2O_5, J. Phys. Soc. Jpn. **70**, 145 (2001).

[15] H. Kimura, S. Kobayashi, S. Wakimoto, Y. Noda, and K. Kohn, Magnetically induced ferroelectricity in multiferroic compounds of RMn_2O_5, Ferroelectrics **354**, 77 (2007).

[16] T. Weißbach, Untersuchungen zu Kristallstruktur und Magnetismus von Übergangsmetalloxiden mittels Dichtefunktionaltheorie und kristallographischer experimenteller Techniken, Ph.D. thesis, Technische Universität Bergakademie Freiberg, 2010.

[17] S. Kobayashi, T. Osawa, H. Kimura, Y. Noda, I. Kagomiya, and K. Kohn, Reinvestigation of simultaneous magnetic and ferroelectric phase transitions in YMn_2O_5, J. Phys. Soc. Jpn. **73**, 1593 (2004).

[18] Y. F. Popov, A. M. Kadomtseva, S. S. Krotov, G. P. Vorob'ev, and M. M. Lukina, Magnetoelectric effect in YMn_2O_5 in strong pulsed magnetic fields, Ferroelectrics **279**, 147 (2002).

[19] A. P. Pyatakov, A. M. Kadomtseva, G. P. Vorob'ev, Y. F. Popov, S. S. Krotov, A. K. Zvezdin, and M. M. Lukina, Nature of unusual spontaneous and field-induced phase transitions in multiferroics RMn_2O_5, J. Magn. Magn. Mater. **321**, 858 (2009).

[20] M. Tachibana, K. Akiyama, H. Kawaji, and T. Atake, Lattice effects in multiferroic RMn_2O_5 (R = Sm–Dy, Y), Phys. Rev. B **72**, 224425 (2005).

[21] L. C. Chapon, P. G. Radaelli, G. R. Blake, S. Park, and S.-W. Cheong, Ferroelectricity induced by acentric spin-density waves in YMn_2O_5, Phys. Rev. Lett. **96**, 097601 (2006).

[22] G. Giovannetti and J. van den Brink, Electronic correlations decimate the ferroelectric polarization of multiferroic $HoMn_2O_5$, Phys. Rev. Lett. **100**, 227603 (2008).

[23] L. C. Chapon, G. R. Blake, M. J. Gutmann, S. Park, N. Hur, P. G. Radaelli, and S.-W. Cheong, Structural anomalies and multiferroic behavior in magnetically frustrated $TbMn_2O_5$, Phys. Rev. Lett. **93**, 177402 (2004).

[24] C. Vecchini, L. C. Chapon, P. J. Brown, T. Chatterji, S. Park, S.-W. Cheong, and P. G. Radaelli, Commensurate magnetic structures of RMn_2O_5 (R = Y, Ho, Bi) determined by single-crystal neutron diffraction, Phys. Rev. B **77**, 134434 (2008).

[25] H. Kimura, S. Kobayashi, Y. Fukuda, T. Osawa, Y. Kamada, Y. Noda, I. Kagomiya, and K. Kohn, Spiral spin structure in the commensurate magnetic phase of multiferroic $R\mathrm{Mn}_2\mathrm{O}_5$, J. Phys. Soc. Jpn. **76**, 074706 (2007).

[26] A. B. Sushkov, R. V. Aguilar, S. Park, S.-W. Cheong, and H. D. Drew, Electromagnons in multiferroic $\mathrm{YMn}_2\mathrm{O}_5$ and $\mathrm{TbMn}_2\mathrm{O}_5$, Phys. Rev. Lett. **98**, 027202 (2007).

[27] R. Masuda, Y. Kaneko, Y. Yamasaki, Y. Tokura, and Y. Takahashi, Role of commensurability of spin order for optical magnetoelectric effect with electromagnons in multiferroic $\mathrm{YMn}_2\mathrm{O}_5$, Phys. Rev. B **96**, 041117(R) (2017).

[28] S. Wakimoto, H. Kimura, Y. Sakamoto, M. Fukunaga, Y. Noda, M. Takeda, and K. Kakurai, Role of magnetic chirality in polarization flip upon a commensurate-incommensurate magnetic phase transition in $\mathrm{YMn}_2\mathrm{O}_5$, Phys. Rev. B **88**, 140403(R) (2013).

[29] S. Baidya, P. Sanyal, H. Das, B. Roessli, T. Chatterji, and T. Saha-Dasgupta, Understanding neutron scattering data in $\mathrm{YMn}_2\mathrm{O}_5$: An effective spin Hamiltonian, Phys. Rev. B **84**, 054444 (2011).

[30] Z. H. Chen, R.-J. Xiao, C. Ma, Y.-B. Qin, H.-L. Shi, Y.-J. Song, Z. Wang, H.-F. Tian, H.-X. Yang, and J.-Q. Li, Electronic structure of $\mathrm{YMn}_2\mathrm{O}_5$ studied by EELS and first-principles calculations, Front. Phys. **7**, 429 (2012).

[31] Y. Noda, H. Kimura, Y. Kamada, T. Osawa, Y. Fukuda, Y. Ishikawa, S. Kobayashi, Y. Wakabayashi, H. Sawa, N. Ikeda, and K. Kohn, Relation between ferroelectric and antiferromagnetic order in $R\mathrm{Mn}_2\mathrm{O}_5$, Phys. B: Condens. Matter **385-386**, 119 (2006).

[32] Y. Noda, H. Kimura, Y. Kamada, Y. Ishikawa, S. Kobayashi, Y. Wakabayashi, H. Sawa, N. Ikeda, and K. Kohn, Lattice modulation in $\mathrm{YMn}_2\mathrm{O}_5$ and $\mathrm{TbMn}_2\mathrm{O}_5$ studied by using synchrotron radiation X-ray, J. Korean Phys. Soc. **51**, 828 (2007).

[33] Y. Noda, H. Kimura, M. Fukunaga, S. Kobayashi, I. Kagomiya, and K. Kohn, Magnetic and ferroelectric properties of multiferroic $R\mathrm{Mn}_2\mathrm{O}_5$, J. Phys.: Condens. Matter **20**, 434206 (2008).

[34] S.-W. Cheong and M. Mostovoy, Multiferroics: A magnetic twist for ferroelectricity, Nat. Mater. **6**, 13 (2007).

[35] M. Deutsch, T. C. Hansen, M. T. Fernández-Díaz, A. Forget, D. Colson, F. Porcher, and I. Mirebeau, Pressure-induced commensurate phase with potential giant polarization in $\mathrm{YMn}_2\mathrm{O}_5$, Phys. Rev. B **92**, 060410(R) (2015).

[36] M. Fukunaga and Y. Noda, Classification and interpretation of the polarization of multiferroic $R\mathrm{Mn}_2\mathrm{O}_5$, J. Phys. Soc. Jpn. **79**, 054705 (2010).

[37] T.-C. Han and J. G. Lin, R-dependent magnetic and structural properties in $R\mathrm{Mn}_2\mathrm{O}_5$ with $R =$ Y, Er, Ho, Dy, and Tb, J. Appl. Phys. **99**, 08J508 (2006).

[38] A. M. Kadomtseva, S. S. Krotov, Y. F. Popov, and G. P. Vorob'ev, Features of the magnetoelectric behavior of the family of multiferroics $R\mathrm{Mn}_2\mathrm{O}_5$ at high magnetic fields (Review), Low Temp. Phys. **32**, 709 (2006).

[39] J.-H. Kim, S.-H. Lee, S. I. Park, M. Kenzelmann, A. B. Harris, J. Schefer, J.-H. Chung, C. F. Majkrzak, M. Takeda, S. Wakimoto, S. Y. Park, S.-W. Cheong, M. Matsuda, H. Kimura, Y. Noda, and K. Kakurai, Spiral spin structures and origin of the magnetoelectric coupling in $\mathrm{YMn}_2\mathrm{O}_5$, Phys. Rev. B **78**, 245115 (2008).

[40] H. Kimura, Y. Noda, and K. Kohn, Spin-driven ferroelectricity in the multiferroic compounds of $R\mathrm{Mn}_2\mathrm{O}_5$, J. Magn. Magn. Mater. **321**, 854 (2009).

[41] K. Mukherjee, K. S. Kumar, and A. Banerjee, Observation of different spin behavior with temperature variation and Cr substitution in a multiferroic compound $\mathrm{YMn}_2\mathrm{O}_5$, Solid State Commun. **153**, 66 (2013).

[42] Y. Noda, Y. Fukuda, H. Kimura, I. Kagomiya, S. Matsumoto, K. Kohn, T. Shoubu, and N. Ikeda, Review and prospect of ferroelectricity and magnetism in $\mathrm{YMn}_2\mathrm{O}_5$, J. Korean Phys. Soc. **42**, S1192 (2003).

[43] Y. F. Popov, A. M. Kadomtseva, S. S. Krotov, G. P. Vorob'ev, K. I. Kamilov, M. M. Lukina, and M. M. Tehranchi, Magnetic and structural phase transitions in $\mathrm{YMn}_2\mathrm{O}_5$ ferromagnetoelectric crystals induced by a strong magnetic field, J. Exp. Theor. Phys. **96**, 961 (2003).

[44] P. G. Radaelli, L. C. Chapon, A. Daoud-Aladine, C. Vecchini, P. J. Brown, T. Chatterji, S. Park, and S.-W. Cheong, Electric field switching of antiferromagnetic domains in $\mathrm{YMn}_2\mathrm{O}_5$: A probe of the multiferroic mechanism, Phys. Rev. Lett. **101**, 067205 (2008).

[45] P. G. Radaelli, C. Vecchini, L. C. Chapon, P. J. Brown, S. Park, and S.-W. Cheong, Incommensurate magnetic structure of $\mathrm{YMn}_2\mathrm{O}_5$, Phys. Rev. B **79**, 020404(R) (2009).

[46] I. Kagomiya, S. Matsumoto, K. Kohn, Y. Fukuda, T. Shoubu, H. Kimura, Y. Noda, and N. Ikeda, Lattice distortion at ferroelectric transition of $\mathrm{YMn}_2\mathrm{O}_5$, Ferroelectrics **286**, 167 (2003).

[47] I. Kagomiya, K.-I. Kakimoto, and H. Ohsato, Precursor phenomenon on ferroelectric transition in multiferroic $\mathrm{YMn}_2\mathrm{O}_5$, J. Eur. Ceram. Soc. **30**, 255 (2010).

[48] A. Inomata and K. Kohn, Pyroelectric effect and possible ferroelectric transition of helimagnetic $\mathrm{GdMn}_2\mathrm{O}_5$, $\mathrm{TbMn}_2\mathrm{O}_5$ and $\mathrm{YMn}_2\mathrm{O}_5$, J. Phys.: Condens. Matter **8**, 2673 (1996).

[49] S. Partzsch, S. B. Wilkins, J. P. Hill, E. Schierle, E. Weschke, D. Souptel, B. Büchner, and J. Geck, Observation of electronic ferroelectric polarization in multiferroic $\mathrm{YMn}_2\mathrm{O}_5$, Phys. Rev. Lett. **107**, 057201 (2011).

[50] C. Richter, M. Zschornak, D. V. Novikov, E. Mehner, M. Nentwich, J. Hanzig, S. Gorfman, and D. C. Meyer, Picometer polar atomic displacements in strontium titanate determined by resonant x-ray diffraction, Nat. Commun. **9**, 178 (2018).

[51] J. Attfield, Resonant powder x-ray diffraction, in *European Powder Diffraction 4*, Materials Science Forum Vol. 228 (Trans Tech, Wollerau, Switzerland, 1996), pp. 201–206.

[52] U. Vainio, K. Pirkkalainen, K. Kisko, G. Goerigk, N. E. Kotelnikova, and R. Serimaa, Copper and copper oxide nanoparticles in a cellulose support studied using anomalous small-angle x-ray scattering, Eur. Phys. J. D **42**, 93 (2007).

[53] C. Richter, D. V. Novikov, E. K. Mukhamedzhanov, M. M. Borisov, K. A. Akimova, E. N. Ovchinnikova, A. P. Oreshko, J. Strempfer, M. Zschornak, E. Mehner, D. C. Meyer, and V. E. Dmitrienko, Mechanisms of the paraelectric to ferroelectric phase transition in $\mathrm{RbH}_2\mathrm{PO}_4$ probed by purely resonant x-ray diffraction, Phys. Rev. B **89**, 094110 (2014).

[54] M. Zschornak, C. Richter, M. Nentwich, H. Stöcker, S. Gemming, and D. C. Meyer, Probing a crystal's short-range structure and local orbitals by resonant x-ray diffraction methods, Cryst. Res. Technol. **49**, 43 (2014).

[55] M. v. Zimmermann, C. S. Nelson, J. P. Hill, D. Gibbs, M. Blume, D. Casa, B. Keimer, Y. Murakami, C.-C. Kao, C.

Venkataraman, T. Gog, Y. Tomioka, and Y. Tokura, X-ray resonant scattering studies of orbital and charge ordering in $Pr_{1-x}Ca_xMnO_3$, Phys. Rev. B **64**, 195133 (2001).

[56] Y. Murakami, H. Kawada, H. Kawata, M. Tanaka, T. Arima, Y. Moritomo, and Y. Tokura, Direct observation of charge and orbital ordering in $La_{0.5}Sr_{1.5}MnO_4$, Phys. Rev. Lett. **80**, 1932 (1998).

[57] V. E. Dmitrienko and E. N. Ovchinnikova, Resonant x-ray diffraction: "Forbidden" Bragg reflections induced by thermal vibrations and point defects, Acta Crystallogr. A **56**, 340 (2000).

[58] B. Bohnenbuck, I. Zegkinoglou, J. Strempfer, C. S. Nelson, H.-H. Wu, C. Schüßler-Langeheine, M. Reehuis, E. Schierle, P. Leininger, T. Herrmannsdörfer, J. C. Lang, G. Srajer, C. T. Lin, and B. Keimer, Magnetic structure of $RuSr_2$ $GdCu_2O_8$ determined by resonant x-ray diffraction, Phys. Rev. Lett. **102**, 037205 (2009).

[59] V. Scagnoli, U. Staub, A. M. Mulders, M. Janousch, G. I. Meijer, G. Hammerl, J. M. Tonnerre, and N. Stojic, Role of magnetic and orbital ordering at the metal-insulator transition in $NdNiO_3$, Phys. Rev. B **73**, 100409(R) (2006).

[60] J. Hanzig, M. Zschornak, F. Hanzig, E. Mehner, H. Stöcker, B. Abendroth, C. Röder, A. Talkenberger, G. Schreiber, D. Rafaja, S. Gemming, and D. C. Meyer, Migration-induced field-stabilized polar phase in strontium titanate single crystals at room temperature, Phys. Rev. B **88**, 024104 (2013).

[61] See Supplemental Material at http://link.aps.org/supplemental/10.1103/PhysRevB.109.054101 for more details about the selections of relevant reflections, the improvement of the fits for dynamic and static displacements for the P phase, the refinement of the CM phase and cif files of the refined structures. The Supplemental Material also contains Refs. [62,63].

[62] G. Liu, W. Wong-Ng, J. A. Kaduk, and L. P. Cook, Interfacial reactions of $Ba_2YCu_3O_{6+z}$ with coated conductor buffer layer, $LaMnO_3$, Physica C **470**, 345 (2010).

[63] C. d. La Calle, J. A. Alonso, M. J. Martínez-Lope, M. García-Hernández, and G. André, Synthesis under high-oxygen pressure, magnetic and structural characterization from neutron powder diffraction data of $YGa_{1-x}Mn_{1+x}O_5$ ($x = 0.23$): A comparison with YMn_2O_5, Mater. Res. Bull. **43**, 197 (2008).

[64] M. Newville, T. Stensitzki, D. B. Allen, M. Rawlik, A. Ingargiola, and A. Nelson, Lmfit: Non-linear least-square minimization and curve-fitting for Python, Astrophysics Source Code Library, record no. ascl:1606.014 (2016).

[65] D. C. Meyer, A. Kupsch, and P. Paufler, Absorption and extinction correction in quantitative DAFS analysis, J. Synchrotron Radiat. **10**, 144 (2003).

[66] K. N. Trueblood, H.-B. Bürgi, H. Burzlaff, J. D. Dunitz, C. M. Gramaccioli, H. H. Schulz, U. Shmueli, and S. C. Abrahams, Atomic displacement parameter nomenclature. Report of a subcommittee on atomic displacement parameter nomenclature, Acta Crystallogr. A **52**, 770 (1996).

[67] D. Souptel, Crystal growth and properties of the novel multiferroic oxide compounds, final technical report for project No. SO840/1, Leibniz Institute for Solid State and Material Research Dresden (2007).

[68] Bruker AXS, Inc., *DOC-M86-EXX190 D8 QUEST User Manual* (Bruker AXS, Madison, Wisconsin, 2012).

[69] E. R. Dobrovinskaya, L. A. Lytvynov, and V. Pishchik, Properties of sapphire, in *Sapphire: Material, Manufacturing, Applications* (Springer, Boston, MA, 2009), pp. 55–176..

[70] R. P. Chaudhury, C. R. dela Cruz, B. Lorenz, Y. Y. Sun, C. W. Chu, S. Park, and S.-W. Cheong, Control of ferroelectric polarization in multiferroic YMn_2O_5 by external pressure, J. Phys.: Conf. Ser. **150**, 042013 (2009).

[71] Honeywell MICRO SWITCH Sensing and Control, Temperature Sensors HEL-700 Series Platinum RTDs (2020), https://docs.rs-online.com/b64b/0900766b800b1e9c.pdf.

[72] M. Fukunaga and Y. Noda, New technique for measuring ferroelectric and antiferroelectric hysteresis loops, J. Phys. Soc. Jpn. **77**, 064706 (2008).

[73] R. Chaudhury, C. R. dela Cruz, B. Lorenz, Y. Sun, C. W. Chu, S. Park, and S.-W. Cheong, Pressure-induced polarization reversal in multiferroic YMn_2O_5, Phys. Rev. B **77**, 220104(R) (2008).

[74] S. D. Brown, L. Bouchenoire, D. Bowyer, J. Kervin, D. Laundy, M. J. Longfield, D. Mannix, D. F. Paul, A. Stunault, P. Thompson, M. J. Cooper, C. A. Lucas, and W. G. Stirling, The XMaS beamline at ESRF: Instrumental developments and high-resolution diffraction studies, J. Synchrotron Radiat. **8**, 1172 (2001).

[75] B. L. Henke, E. M. Gullikson, and J. C. Davis, X-ray interactions: photoabsorption, scattering, transmission, and reflection at $e = 50–30{,}000$ eV, $z = 1—92$, At. Data Nucl. Data Tables **54**, 181 (1993).

[76] M. Renninger, "Umweganregung," eine bisher unbeachtete Wechselwirkungserscheinung bei Raumgitterinterferenzen, Z. Phys. **106**, 141 (1937).

[77] M. Nentwich, M. Zschornak, T. Weigel, T. Köhler, D. Novikov, D. C. Meyer, and C. Richter, Treatment of multiple beam x-ray diffraction in energy dependent measurements, J. Synchrotron Radiat. **31**, 28 (2024).

[78] C. Richter, pyasf: Symbolic computing of anisotropic resonant scattering factor, GitHub repository, https://github.com/carichte/pyasf (2023).

[79] Y. Avni, Energy spectra of x-ray clusters of galaxies, Astrophys. J. **210**, 642 (1976).

[80] V. R. A. Dubach and A. Guskov, The resolution in x-ray crystallography and single-particle cryogenic electron microscopy, Crystals **10**, 580 (2020).

[81] G. M. Sheldrick, Phase annealing in SHELX-90: Direct methods for larger structures, Acta Crystallogr. A **46**, 467 (1990).

[82] V. Balédent, S. Chattopadhyay, P. Fertey, M. B. Lepetit, M. Greenblatt, B. Wanklyn, F. O. Saouma, J. I. Jang, and P. Foury-Leylekian, Evidence for room temperature electric polarization in RMn_2O_5 multiferroics, Phys. Rev. Lett. **114**, 117601 (2015).

[83] G. R. Blake, L. C. Chapon, P. G. Radaelli, S. Park, N. Hur, S. W. Cheong, and J. Rodriguez-Carvajal, Spin structure and magnetic frustration in multiferroic RMn_2O_5 ($R =$ Tb, Ho, Dy), Phys. Rev. B **71**, 214402 (2005).

[84] W. Peng, V. Balédent, C. V. Colin, T. C. Hansen, M. Greenblatt, and P. Foury-Leylekian, Tuning competing

magnetic interactions with pressure in $R\mathrm{Mn}_2\,\mathrm{O}_5$ multiferroics, Phys. Rev. B **99**, 245109 (2019).

[85] Y. Ishii, S. Horio, M. Mitarashi, T. Sakakura, M. Fukunaga, Y. Noda, T. Honda, H. Nakao, Y. Murakami, and H. Kimura, Observation of magnetic order in multiferroic $\mathrm{SmMn}_2\mathrm{O}_5$ studied by resonant x-ray magnetic scattering, Phys. Rev. B **93**, 064415 (2016).

[86] B. Roessli, P. Fischer, P. J. Brown, M. Janoschek, D. Sheptyakov, S. N. Gvasaliya, B. Ouladdiaf, O. Zaharko, E. Golovenchits, and V. Sanina, Noncentrosymmetric commensurate magnetic ordering of multiferroic $\mathrm{ErMn}_2\mathrm{O}_5$, J. Phys.: Condens. Matter **20**, 485216 (2008).

[87] N. Narayanan, P. J. Graham, P. Rovillain, J. O'Brien, J. Bertinshaw, S. Yick, J. Hester, A. Maljuk, D. Souptel, B. Büchner, D. Argyriou, and C. Ulrich, Reduced crystal symmetry as the origin of the ferroelectric polarization within the incommensurate magnetic phase of $\mathrm{TbMn}_2\mathrm{O}_5$, Phys. Rev. B **105**, 214413 (2022).

[88] C. Wang, G.-C. Guo, and L. He, Ferroelectricity driven by the noncentrosymmetric magnetic ordering in multiferroic $\mathrm{TbMn}_2\mathrm{O}_5$: A first-principles study, Phys. Rev. Lett. **99**, 177202 (2007).

[89] C. Wang, G.-C. Guo, and L. He, First-principles study of the lattice and electronic structure of $\mathrm{TbMn}_2\mathrm{O}_5$, Phys. Rev. B **77**, 134113 (2008).

[90] I. Radulov, V. I. Nizhankovskii, V. Lovchinov, D. Dimitrov, and A. Apostolov, Colossal magnetostriction effect in $\mathrm{HoMn}_2\mathrm{O}_5$, Eur. Phys. J. B **52**, 361 (2006).

[91] T. Weigel, C. Ludt, T. Leisegang, E. Mehner, S. Jachalke, H. Stöcker, T. Doert, D. C. Meyer, and M. Zschornak, Spontaneous polarization and pyroelectric coefficient of lithium niobate and lithium tantalate determined from crystal structure data, Phys. Rev. B **108**, 054105 (2023).

[92] Q. Peng and R. E. Cohen, Origin of pyroelectricity in LiNbO_3, Phys. Rev. B **83**, 220103(R) (2011).

[93] R. Resta, Macroscopic polarization in crystalline dielectrics: The geometric phase approach, Rev. Mod. Phys. **66**, 899 (1994).

[94] R. D. King-Smith and D. Vanderbilt, Theory of polarization of crystalline solids, Phys. Rev. B **47**, 1651 (1993).

[95] D. Vanderbilt and R. D. King-Smith, Electric polarization as a bulk quantity and its relation to surface charge, Phys. Rev. B **48**, 4442 (1993).

[96] S. Partzsch, S. B. Wilkins, E. Schierle, J. E. Hamann-Borrero, H. Wadati, V. Soltwisch, J. P. Hill, E. Weschke, D. Souptel, B. Büchner, and J. Geck, Resonant soft x-ray scattering studies of multiferroic $\mathrm{YMn}_2\mathrm{O}_5$, Eur. Phys. J.: Spec. Top. **208**, 133 (2012).

[97] K. Gautam, A. Ahad, K. Dey, S. S. Majid, S. Francoual, V. G. Sathe, I. da Silva, and D. K. Shukla, Symmetry breaking and spin lattice coupling in $\mathrm{NdCrTiO}_5$, Phys. Rev. B **100**, 104106 (2019).

[98] B. Lorenz, Hexagonal manganites-($R\mathrm{MnO}_3$): Class (i) multiferroics with strong coupling of magnetism and ferroelectricity, International Scholarly Research Notices **2013**, 497073 (2013).

[99] J. Su, Z. Z. Yang, X. M. Lu, J. T. Zhang, L. Gu, C. J. Lu, Q. C. Li, J.-M. Liu, and J. S. Zhu, Magnetism-driven ferroelectricity in double perovskite $\mathrm{Y}_2\mathrm{NiMnO}_6$, ACS Appl. Mater. Interfaces **7**, 13260 (2015).

[100] G. Lawes, A. B. Harris, T. Kimura, N. Rogado, R. J. Cava, A. Aharony, O. Entin-Wohlman, T. Yildrim, M. Kenzelmann, C. Broholm, and A. P. Ramirez, Magnetically driven ferroelectric order in $\mathrm{Ni}_3\mathrm{V}_2\mathrm{O}_8$, Phys. Rev. Lett. **95**, 087205 (2005).

[101] R. Saha, A. Sundaresan, and C. R. Rao, Novel features of multiferroic and magnetoelectric ferrites and chromites exhibiting magnetically driven ferroelectricity, Mater. Horiz. **1**, 20 (2014).

[102] D. Meier and S. M. Selbach, Ferroelectric domain walls for nanotechnology, Nat. Rev. Mater. **7**, 157 (2022).

[103] IUCr, *International Tables for Crystallography, Volume A: Space Group Symmetry*, 5th ed., edited by T. Hahn, International Tables for Crystallography (Kluwer, Dordrecht, 2002).

[104] I. Kagomiya, M. Yoshino, S. Matsumoto, Y. Seki, and K. Kohn, *Ferroelectric Transition of Helimagnetic* $R\mathrm{Mn}_2\mathrm{O}_5$, in *Proceedings of the Eighth International Conference on Ferrite* (Japan Society of Powder and Powder Metallurgy, 2000), p. 229.

[105] P. J. Brown, A. G. Fox, E. N. Maslen, M. A. O'Keefe, and B. T. M. Willis, Intensity of diffracted intensities, in *International Tables of Crystallography* (Springer Dordrecht, Netherlands, 2006), Vol. C, Chap. 6.1, p. 554.

[106] V. Lucarini, J. J. Saarinen, and K.-E. Peiponen, Multiply subtractive generalized Kramers-Kronig relations: Application on third-harmonic generation susceptibility on polysilane, J. Chem. Phys. **119**, 11095 (2003).

[107] C. Richter, Applications of resonant hard x-ray diffraction for characterization of structural modifications in crystals, Ph.D. thesis, TU Bergakademie Freiberg, 2017.

[108] S. Sasaki, Numerical tables of anomalous scattering factors calculated by the Cromer and Liberman's method, Tech. Rep. No. KEK–88-14, National Laboratory for High Energy Physics, 1989.

[109] W. Massa, *Kristallstrukturbestimmung*, 7th ed. (Vieweg & Teubner, Wiesbaden, 2011).

[110] S. Jachalke, E. Mehner, H. Stöcker, J. Hanzig, M. Sonntag, T. Weigel, T. Leisegang, and D. C. Meyer, How to measure the pyroelectric coefficient? Appl. Phys. Rev. **4**, 021303 (2017).

[111] G. Kresse and D. Joubert, From ultrasoft pseudopotentials to the projector augmented-wave method, Phys. Rev. B **59**, 1758 (1999).

[112] J. P. Perdew, K. Burke, and M. Ernzerhof, Generalized gradient approximation made simple, Phys. Rev. Lett. **77**, 3865 (1996).

[113] H. J. Monkhorst and J. D. Pack, Special points for Brillouin-zone integrations, Phys. Rev. B **13**, 5188 (1976).